Elastic full-waveform inversion in attenuative and anisotropic media applied to walk-away vertical seismic profile data

Wenyong Pan, Kris Innanen

ABSTRACT

Viscoelastic full-waveform inversion (FWI) is applied to walk-away vertical seismic profile (W-VSP) data acquired at a producing heavy-oil field in Western Canada, for the determination of subsurface velocity models (P-wave velocity α and S-wave velocity β) and attenuation models (P-wave quality factor Q_α and S-wave quality factor Q_β). To mitigate strong velocity-attenuation tradeoffs, a two-stage approach is adopted. In stage-I, α and β models are first inverted using a standard waveform-difference (WD) misfit function. Following this, in stage-II, different amplitude-based misfit functions are used to estimate the Q_α and Q_β models. Compared to the traditional WD misfit function, the amplitude-based misfit functions show stronger sensitivity to attenuation anomalies and appear to be able to invert Q_α and Q_β models more reliably in the presence of velocity errors. Overall, the root-mean-square amplitude-ratio and spectral amplitude-ratio misfit functions outperform other misfit function choices. In the final outputs of our inversion experiments, significant drops in both α to β ratio ($\sim$ 1.6) and Poisson's ratio ($\sim$ 0.23) are apparent within the Clearwater formation (depth $\sim$ 0.45-0.5 km) of Mannville Group in Western Canada Sedimentary Basin. Strong Q_α ($\sim$ 20) and Q_β ($\sim$ 15) anomalies are also evident in this zone. These observations provide informative inferences to identify the target attenuative reservoir saturated with heavy-oil resources. In the final section of this report, anisotropic-elastic FWI in vertical transverse isotropic (VTI) media with different model parameterizations are applied to this W-VSP data.

INTRODUCTION

Full-waveform inversion (FWI) has been widely studied in exploration geophysics (Tarantola, 1984; Pratt et al., 1998; Virieux and Operto, 2009; Brossier et al., 2009; Leeuwen and Mulder, 2010; Guitton and Díaz, 2012; Warner et al., 2013; Yang et al., 2014; Yuan and Simons, 2014; Routh et al., 2017; Pan et al., 2018b; Yao et al., 2018) and global seismology (Tromp et al., 2005; Liu and Tromp, 2006; Tape et al., 2009; Zhu and Tromp, 2013; Zhu et al., 2013; Bozdağ et al., 2016) and is now regularly applied to produce high-resolution subsurface velocity structures. When the seismic waves propagate in real geological volumes, the amplitude and phase of the waveforms are affected by processes of dissipation and dispersion (Liu et al., 1976; Carcione et al., 1988a; Robertsson et al., 1994). Ignoring attenuation and dispersion may produce biased velocity estimations in FWI. Reliable estimation of subsurface attenuation parameters is critical, both for compensation of the amplitude and phase distortions in seismic imaging (Innanen and Lira, 2010; Margrave et al., 2011; Zhu, 2014; Zhu et al., 2014; Dutta and Schuster, 2014; Zhu and Harris, 2015; Guo et al., 2016; Guo and McMechan, 2018; Shen et al., 2018a,b), and for interpretation – attenuation parameters can provide independent constraints on the rock/fluid properties of the reservoir target (Innanen, 2011; Moradi and Innanen, 2015; Chen and Innanen, 2018). Estimating attenuation models from seismic waves is a challenging task. Conventionally, the spectral-ratio (SR) (Bath, 1974) and central-frequency shift (CFS) (Quan and Harris, 1997) methods can be used to estimate the attenuation values. However, the SR and CFS methods are especially sensitive to noise and data variations not obeying assumed statistics (Tonn, 1991), and, because they are ray-based, may provide unrealistic attenuation models in the areas with complex geological structures. There are thus at least two motivating factors to include attenuation within FWI: to suppress bias in velocity estimation, and to construct interpretable attenuation models, invoking the same degree of wave-theoretic completeness used for the velocities.

In a linear viscoelastic model, the anelastic effects are often quantified by the quality factor Q. Wave propagation in viscoelastic media can be simulated using the generalized standard linear solid (GSLS) model (Carcione et al., 1988a,b; Robertsson et al., 1994; Blanch et al., 1995; Komatitsch and Tromp, 2005). In the numerical simulation based on GSLS model, the convolution stress-strain relationship is approximated with a set of discretized partial differential equations that accommodate arbitrary spatial Q distributions. Thus, an FWI scheme can be set up to invert the attenuation parameters alongside other elastic properties by solving the visco-elastodynamic wave equation. One difficulty of inverting attenuation parameters using FWI is known as the interparameter tradeoff problem. When simultaneously inverting multiple physical parameters, the errors in one physical parameter tend to be mapped into the estimation of others (Operto et al., 2013; Innanen, 2014; Alkhalifah and Plessix, 2014; Pan et al., 2016, 2018a; Chen and Sacchi, 2018; Pan et al., 2019). These errors lead to artifacts in the inverted models. Different strategies have been developed to reduce interparameter tradeoffs in viscoacoustic FWI. Kamei and Pratt (2013) introduced a scaling term to control the magnitudes of the attenuation model updates for reducing the parameter crosstalk artifacts in viscoacoustic FWI. Métivier et al. (2015), Keating and Innanen (2018) and Yang et al. (2018) used Newton-based optimization methods, which, at increased computational cost, account for the parameter crosstalks with approximations of the inverse multiparameter Hessian. The problem may also be approached with alternative misfit function definitions; for instance, Dutta and Schuster (2016) designed an central-frequency misfit function for wave-equation Q tomography. It is also not at present clear under which circumstances attenuation parameters should be inverted for simultaneously alongside elastic properties, and under which circumstances velocities and attenuation parameters should be determined sequentially (for an analysis of this issue in the context of 3D viscoacoustic FWI, see Operto and Miniussi, 2018).

Most published viscoelastic FWI studies are theoretical analyses and synthetic experiments (Brossier, 2011; Fichtner and van Driel, 2014; Fabien-Ouellet et al., 2017; Bai et al., 2017; Trinh et al., 2018); results from field applications need to increase before the optimal workflow is identified. In this paper, we apply viscoelastic FWI to the walk-away vertical seismic profile (W-VSP) data acquired at a producing heavy-oil field in Western Canada, with the aim of determining elastic velocity models (P-wave velocity α and S-wave velocity β) and attenuation models (P-wave quality factor Q_α and S-wave quality factor Q_β). The forward modelling problem in viscoelastic media is solved in the time domain with a spectral-element method based on the GSLS model (Komatitsch and Tromp, 2005). The velocity sensitivity kernels are calculated efficiently with the adjoint-state method (Tromp et al., 2005; Liu and Tromp, 2006; Plessix, 2006). Because the quality factor Q is not explicitly incorporated in the time domain visco-elastodynamic wave equation, following Tromp et al. (2005), we calculate the attenuation sensitivity kernels by introducing additional adjoint sources with the assumption of frequency-independent Q. To reduce the influence of velocity errors on the determination of attenuation parameters, we introduce and consider several candidate amplitude-based misfit functions, including instantaneous amplitude-ratio (I-AR), root-mean-square amplitude-ratio (RMS-AR) and spectral amplitude-ratio (S-AR), to estimate the Q_α and Q_β models. Compared to the standard waveform-difference (WD) misfit function, these amplitude-based misfit functions are designed to accentuate the importance of attenuation over velocity on the seismic data, and thus may lead to more reliable Q model building, in particular with weaker interparameter tradeoffs. Synthetic examples are used to verify the stronger sensitivity of the amplitude-based misfit functions to attenuation anomalies in the presence of velocity errors.

For the W-VSP data application, the workflow is as follows. We first create α and β starting models from the well-log data. Then, averaged Q_α and Q_β values estimated using the traditional SR and CFS methods are used to build the Q_α and Q_β starting models. We then begin a two-stage sequential viscoelastic FWI process. In stage-I, the α and β models are inverted using a standard WD misfit function. High-resolution α and β models are obtained. At the depth of 0.45-0.5 km, the Clearwater formation of lower Mannville Group in Western Canada Sedimentary Basin, we observe obvious reductions of α to β ratio ($\alpha/\beta \sim$ 1.6) and Poisson's ratio ($\nu \sim$ 0.23) models indicating potential sandstone deposits, in agreement with earlier elastic FWI studies (Pan et al., 2018b). In stage-II, we employ the amplitude-based misfit functions to estimate the Q_α and Q_β models compared to the traditional WD misfit function. Overall, the RMS-AR and S-AR misfit functions show comparable inversion performance, and between them appear to outperform the other misfit function choices, in providing attenuation models which match expectations based on the reservoir geology. In the final inverted attenuation models, we observe strong Q_α ($\sim$ 20) and Q_β ($\sim$ 15) anomalies in the target Clearwater formation. This represents an important complement to the velocity models for identifying and characterizing the reservoir formation.

Ignoring anisotropic effects may produced distorted velocity formations. In the final section this report, the anisotropic-elastic FWI in vertical transverse isotropic (VTI) media with four different model parameterizations, are applied to this W-VSP data. The inversion results show that incorporating anisotropy in elastic FWI produces models with more continuous and coherent geological formations.

This paper is organized as follows. The basic principle of forward modelling in viscoelastic media based on GSLS model and adjoint viscoelastic FWI are reviewed. The three amplitude-based misfit functions are then introduced. Synthetic example is given to verify the stronger resolving ability of the amplitude-based misfit functions for attenuation estimation in the presence of velocity errors. In the field data application section, we introduce the geological background of the studied area, data preparation and the inversion workflow. Then the two-stage inversion strategy is used to invert the velocity and attenuation model sequentially. The inversion results are interpreted to characterize the target heavy-oil reservoir. Finally, anisotropic-elastic FWI with different model parameterizations are applied to this W-VSP data.

FORWARD MODELLING IN VISCOELASTIC MEDIA BASED ON GSLS MODEL

We simulate the wave propagation in viscoelastic media based on the common generalized standard linear solid (GSLS) model (Carcione et al., 1988a,b; Robertsson et al., 1994; Blanch et al., 1995; Komatitsch and Tromp, 2005). In a linear anisotropic viscoelastic medium, the momentum conservation law is given by

$$\rho\left(\mathbf{x}\right)\ddot{u}_i\left(\mathbf{x},t\right)+\partial_j\sigma_{ij}\left(\mathbf{x},t\right)=f_i\left(\mathbf{x}_s\right), \tag{1}$$

where ρ is the mass density, u_i is the ith component displacement field at subsurface location **x** and time t, the symbol "$\ddot{}$" means the second-order time derivative, f_i represents the source term in the ith direction at location $\mathbf{x}_s$, and the stress tensor σ_{ij} is determined by the entire history of the strain field (Aki and Richards, 2002; Dahlen and Tromp, 1998):

$$\sigma_{ij}\left(\mathbf{x},t\right)=\int_0^t c_{ijkl}\left(\mathbf{x},t-t''\right)\dot{\varepsilon}_{kl}\left(\mathbf{x},t''\right)dt'', \tag{2}$$

where ε_{kl} is the strain tensor, the symbol "$\dot{}$" denotes the first-order time derivative, and the fourth-order tensor c_{ijkl} (with i, j, k, l taking on the values of x, y, z) determines the medium attenuation, and can be simulated by a GSLS model with several parallel relaxation mechanisms. In general anisotropic media, the relaxation function is given by

$$c_{ijkl}\left(\mathbf{x},t\right)=c_{ijkl}^R\left(\mathbf{x},+\infty\right)\left[1+\tau_{ijkl}\frac{1}{P}\sum_{p=1}^{P}\mathbf{exp}\left(-\frac{t}{\tau^{\sigma p}}\right)\right]H\left(t\right), \tag{3}$$

where c_{ijkl}^R is the relaxed stiffness, P is the maximum number of relaxation mechanisms, $H(t)$ is the Heaviside function, and τ_{ijkl} determines the attenuation magnitude (Blanch et al., 1995):

$$\tau_{ijkl}=\frac{\tau_{ijkl}^{\varepsilon p}}{\tau^{\sigma p}}-1, \tag{4}$$

where $\tau_{ijkl}^{\varepsilon p}$ and $\tau^{\sigma p}$ are the strain and stress relaxation times of the pth relaxation mechanism. The convolution in the constitutive relation can be eliminated by taking time derivative of equation (2):

$$\dot{\sigma}_{ij}\left(\mathbf{x},t\right)=c_{ijkl}^R\left(\mathbf{x},+\infty\right)\left(\tau_{ijkl}+1\right)\dot{\varepsilon}_{kl}\left(\mathbf{x},t\right)-c_{ijkl}^R\left(\mathbf{x},+\infty\right)\tau_{ijkl}\sum_{p=1}^{P}\epsilon_{kl}^p\left(\mathbf{x},t\right), \tag{5}$$

where ϵ_{kl}^p are the memory strain variables

$$\epsilon_{kl}^p\left(\mathbf{x},t\right)=\frac{1}{P\tau^{\sigma p}}\int_0^t\mathbf{exp}\left(-\frac{t-t''}{\tau^{\sigma p}}\right)H\left(t-t''\right)\dot{\varepsilon}_{kl}\left(\mathbf{x},t''\right)dt'', \tag{6}$$

satisfying the equation

$$\dot{\epsilon}_{kl}^p\left(\mathbf{x},t\right)=-\frac{1}{\tau^{\sigma p}}\epsilon_{kl}^p\left(\mathbf{x},t\right)+\frac{1}{P\tau^{\sigma p}}\dot{\varepsilon}_{kl}\left(\mathbf{x},t\right). \tag{7}$$

The convolution operation within the constitutive relation is in this way replaced with a set of partial differential equations. Using a superposition of relaxation mechanisms, wave propagation in an attenuating medium with arbitrary spatial distributions of quality factors can be simulated.

VISCOELASTIC FULL-WAVEFORM INVERSION WITH THE ADJOINT-STATE METHOD

In traditional seismic FWI, the model properties are estimated iteratively by minimizing the differences between the seismic observation u_i^{obs} and synthetic seismogram u_i, which we will refer to in this paper as the waveform-difference (WD) misfit function. The inverse problem is solved subject to equation (1), which leads to the following augmented Lagrangian misfit function:

$$\tilde{\chi}^{\text{WD}}(\mathbf{m}) = \frac{1}{2}\sum_{\mathbf{x}_r}\int_0^{t'}\left[u_i(\mathbf{x}_r,t;\mathbf{m}) - u_i^{\text{obs}}(\mathbf{x}_r,t)\right]^2 dt + \int_0^{t'}\int_\Omega \lambda_i(\mathbf{x},t)\left[\rho(\mathbf{x})\ddot{u}_i(\mathbf{x},t) + \partial_j\left(\int_0^t c_{ijkl}(\mathbf{x},t-t'')\dot{\varepsilon}_{kl}(\mathbf{x},t'')\,dt''\right) - f_i(\mathbf{x}_s)\right]d\mathbf{x}dt, \tag{8}$$

where $\mathbf{x}_r$ indicates receiver location, t' is the maximum recording time, $\mathbf{m}$ is the model property vector, Ω denotes all contributing space and λ_i is the Lagrangian multiplier. The variation of the misfit function associated with perturbations in density ρ and elastic stiffness tensor c_{ijkl} has the form (Liu and Tromp, 2008; Fichtner and van Driel, 2014)

$$\Delta\tilde{\chi}^{\text{WD}} = -\int_0^{t'}\int_\Omega \Delta\rho(\mathbf{x})\,u_i^\dagger(\mathbf{x},t'-t)\,\ddot{u}_i(\mathbf{x},t)\,d\mathbf{x}dt - \int_0^{t'}\int_\Omega\left[\int_0^{t'-t}\Delta c_{ijkl}(\mathbf{x},t'-t-t'')\,\dot{\varepsilon}_{ij}^\dagger(\mathbf{x},t'')\,dt''\right]\varepsilon_{kl}(\mathbf{x},t)\,d\mathbf{x}dt, \tag{9}$$

where $u_i^\dagger$ and $\varepsilon_{ij}^\dagger$ are the adjoint displacement and strain fields defined as the time-reversed Lagrangian displacement field λ_i and strain field $\mathfrak{e}_{kl} = \partial_l\lambda_k$. These can be obtained by solving the adjoint-state equation

$$\rho(\mathbf{x})\ddot{\lambda}_i(\mathbf{x},t) - \partial_j\left[\int_0^t c_{ijkl}(\mathbf{x},t-t'')\,\dot{\mathfrak{e}}_{kl}(\mathbf{x},t'')\,dt''\right] = f_{i,\text{WD}}^\dagger(\mathbf{x},t), \tag{10}$$

where $f_{i,\text{WD}}^\dagger$ is the regular adjoint source for the WD misfit function:

$$f_{i,\text{WD}}^\dagger(\mathbf{x},t) = -\sum_{\mathbf{x}_r}\left[u_i(\mathbf{x}_r,t;\mathbf{m}) - u_i^{\text{obs}}(\mathbf{x}_r,t)\right]\delta(\mathbf{x}-\mathbf{x}_r). \tag{11}$$

In isotropic viscoelastic media, the relaxation function simplifies to $c_{ijkl} = \left(\kappa - \frac{2}{3}\mu\right)\delta_{ij}\delta_{kl} + \mu\left(\delta_{ik}\delta_{jl} + \delta_{jk}\delta_{il}\right)$, where δ_{ij} is the Kronecker delta function, and κ and μ are the bulk modulus and shear modulus, respectively. Variation of the misfit function is re-formulated as

$$\Delta\tilde{\chi}^{\text{WD}} = \int_\Omega\left[a_\rho(\mathbf{x})K_\rho(\mathbf{x}) + a_\kappa(\mathbf{x})K_\kappa(\mathbf{x}) + a_\mu(\mathbf{x})K_\mu(\mathbf{x})\right]d\mathbf{x}, \tag{12}$$

where $a_\rho = \Delta\rho/\rho$, $a_\kappa = \Delta\kappa/\kappa$ and $a_\mu = \Delta\mu/\mu$ are the relative model perturbations of ρ, κ and μ. K_ρ, K_κ and K_μ are the corresponding sensitivity kernels:

$$K_\rho = - \ll \rho u_i^\dagger \ddot{u}_i \gg, \tag{13a}$$

$$K_\kappa = - \ll \left(\kappa * \dot{\varepsilon}_{ii}^\dagger\right) \varepsilon_{kk} \gg, \tag{13b}$$

$$K_\mu = - \ll \left[\left(\delta_{ik}\delta_{jl} + \delta_{jk}\delta_{il} - \frac{2}{3}\delta_{ij}\delta_{kl}\right) \mu * \dot{\varepsilon}_{ij}^\dagger\right] \varepsilon_{kl} \gg, \tag{13c}$$

where $*$ denotes time convolution, and the summations over volume, time, sources and receivers are replaced with the symbol $\ll \cdot \gg$. The attenuation and dispersion effects are often quantified with the quality factor Q. However, Q is not explicitly incorporated in the time domain visco-elastodynamic wave equation, which complicates the derivation of the attenuation sensitivity kernels. In this paper, we derive the attenuation sensitivity kernels following Tromp et al. (2005). Within the exploration geophysics frequency band (approximately $1 \sim 200$ Hz), Q is nearly constant; within this approximation the bulk modulus and shear modulus quality factors (Q_κ and Q_μ) can be written as (Liu et al., 1976; Dahlen and Tromp, 1998; Tromp et al., 2005):

$$\kappa(\omega) = \kappa(\omega_0)\left[1 + \frac{2}{\pi Q_\kappa}\ln\frac{|\omega|}{\omega_0} - \mathbf{i}\mathrm{sgn}(\omega)\frac{1}{Q_\kappa}\right], \tag{14a}$$

$$\mu(\omega) = \mu(\omega_0)\left[1 + \frac{2}{\pi Q_\mu}\ln\frac{|\omega|}{\omega_0} - \mathbf{i}\mathrm{sgn}(\omega)\frac{1}{Q_\mu}\right], \tag{14b}$$

where ω indicates the angular frequency, ω_0 is the reference angular frequency, $\mathbf{i}$ denotes the complex unit, and $\mathrm{sgn}(\omega)$ denotes the sign of ω. Within the GSLS model, several standard linear solid systems at specific reference frequencies can be used to fit a constant Q value within the seismic frequency band. The Fréchet derivative sensitive kernels for Q_κ and Q_μ are given by

$$K_{Q_\kappa} = -\frac{K_\kappa^{Q_\kappa}}{Q_\kappa}, K_{Q_\mu} = -\frac{K_\mu^{Q_\mu}}{Q_\mu}, \tag{15}$$

where the kernels $K_\kappa^{Q_\kappa}$ and $K_\mu^{Q_\mu}$ are the same as K_κ and K_μ but invoking different adjoint source $f_{i,Q}^\dagger$:

$$f_{i,Q}^\dagger(\mathbf{x}, t) = \frac{1}{2\pi}\int_{-\infty}^{+\infty}\left[\frac{2}{\pi}\ln\frac{|\omega|}{\omega_0} - \mathbf{i}\mathrm{sign}(\omega)\right]\tilde{f}_{i,\mathrm{WD}}^\dagger(\mathbf{x}, \omega)\,\mathbf{exp}(\mathbf{i}\omega t)\,d\omega, \tag{16}$$

where $\tilde{f}_{i,\mathrm{WD}}^\dagger$ is the Fourier transform of the regular adjoint source for the WD misfit function. In this paper, we describe the viscoelastic media with density ρ', P-wave velocity α, S-wave velocity β, P-wave quality factor Q_α and S-wave quality factor Q_β. The velocity quality factors Q_α and Q_β are related to the modulus quality factors Q_κ and Q_μ by (Dahlen and Tromp, 1998)

$$Q_\kappa = \frac{\alpha^2 - \beta^2}{\alpha^2 Q_\alpha^{-1} - \beta^2 Q_\beta^{-1}}, Q_\mu = Q_\beta. \tag{17}$$

The corresponding sensitivity kernels for ρ', α, β, Q_α and Q_β are then

$$K_{\rho'} = K_\rho + K_\kappa + K_\mu, \tag{18a}$$

$$K_\alpha = 2\left(1+\frac{4\beta^2}{3\alpha^2-4\beta^2}\right)K_\kappa + \left(\frac{2\alpha^2}{\alpha^2-\beta^2} - \frac{2\alpha^2 Q_\beta}{\alpha^2 Q_\beta - \beta^2 Q_\alpha}\right)K_{Q_\kappa}, \tag{18b}$$

$$K_\beta = 2\left(K_\mu - \frac{4\beta^2}{3\alpha^2-4\beta^2}K_\kappa\right) + \left(\frac{2\beta^2 Q_\alpha}{\alpha^2 Q_\beta - \beta^2 Q_\alpha} - \frac{2\beta^2}{\alpha^2-\beta^2}\right)K_{Q_\kappa}, \tag{18c}$$

$$K_{Q_\alpha} = \left(\frac{\alpha^2}{\alpha^2-\beta^2} + \frac{\beta^2 Q_\alpha}{Q_\beta \alpha^2 - \beta^2 Q_\alpha}\right)K_{Q_\kappa}, \tag{18d}$$

$$K_{Q_\beta} = K_{Q_\mu}. \tag{18e}$$

At each nonlinear iteration of the inversion process, the model is updated by:

$$\mathbf{m}_{\tilde{k}+1} = \mathbf{m}_{\tilde{k}} - \tilde{\mu}_{\tilde{k}} \Delta \mathbf{m}_{\tilde{k}}, \tag{19}$$

where $\tilde{\mu}_{\tilde{k}}$ and $\Delta \mathbf{m}_{\tilde{k}}$ are the step length, calculated with a line search (Nocedal and Wright, 2006) and the search direction of the $\tilde{k}$th iteration. The L-BFGS method is used to construct the search direction for model updating at each nonlinear iteration (Nocedal and Wright, 2006).

AMPLITUDE-BASED MISFIT FUNCTIONS

Sequential inversion strategy is employed to invert the elastic velocities and attenuation parameters with alternative misfit functions, which accentuate the influences of different physical parameters on the data. Attenuation results in both phase and amplitude changes of the waveforms as the seismic wave propagates. However, traveltime, and, at moderate frequencies, the phase, of the seismic data are mainly controlled by the velocity perturbations. The influence of attenuation is more pronounced on seismic amplitudes. For this reason we attempt a sequential viscoelastic FWI using amplitude-based misfit functions for estimating the subsurface attenuation models.

Instantaneous amplitude-ratio misfit function

The envelope attribute measures the strength of the seismic signal at a particular instant (through the instantaneous amplitude). Following Bozdağ et al. (2011), we define the instantaneous amplitude-ratio (I-AR) misfit function as the squared logarithmic ratio of the envelope of the observed and synthetic data:

$$\chi^{\text{I-AR}}(\mathbf{m}) = \frac{1}{2}\sum_{\mathbf{x}_r}\int_0^{t'} \left[\ln \frac{E_i^{\text{obs}}(\mathbf{x}_r, t)}{E_i(\mathbf{x}_r, t; \mathbf{m})}\right]^2 dt, \tag{20}$$

where ln is the natural logarithm, and E_i^{obs} and E_i represent the envelopes of the observed and synthetic data respectively. The regular adjoint source of the I-AR misfit function is given by

$$\begin{aligned} f_{i,\text{I-AR}}^{\dagger}(\mathbf{x}, t) = -\sum_{\mathbf{x}_r}\Bigg\{ & \ln\left[\frac{E_i^{\text{obs}}(\mathbf{x}_r, t)}{E_i(\mathbf{x}_r, t; \mathbf{m})}\right] \frac{\mathrm{w}(t)\, u_i(\mathbf{x}_r, t; \mathbf{m})}{E_i^2(\mathbf{x}_r, t; \mathbf{m})} \\ & + \mathcal{H}\left[\ln\left[\frac{E_i^{\text{obs}}(\mathbf{x}_r, t)}{E_i(\mathbf{x}_r, t; \mathbf{m})}\right] \frac{\mathcal{H}[\mathrm{w}(t)\, u_i(\mathbf{x}_r, t; \mathbf{m})]}{E_r^2(\mathbf{x}_r, t; \mathbf{m})}\right]\Bigg\}\, \delta(\mathbf{x} - \mathbf{x}_r), \end{aligned} \tag{21}$$

where $\mathcal{H}$ indicates the Hilbert transform. To calculate the attenuation sensitivity kernels, we need another different adjoint source, which can be obtained by replacing the Fourier transform of the adjoint source $f_{i,\mathrm{WD}}^{\dagger}$ in equation (16) with the Fourier transform of the adjoint source $f_{i,\text{I-AR}}^{\dagger}$.

Root-mean-square amplitude-ratio misfit function

The root-mean-square (RMS) amplitude measures the energy variation of the seismic data within a time period and captures the amplitude loss of the seismic data caused by attenuation. Following Dahlen and Baig (2002), Tromp et al. (2005) and Bozdağ et al. (2011), we introduce the RMS amplitude-ratio (RMS-AR) misfit function defined as the squared logarithmic ratio of RMS amplitude of the observed and synthetic data:

$$\chi^{\text{RMS-AR}}(\mathbf{m}) = \frac{1}{2}\sum_{\mathbf{x}_r}\left[\ln\frac{A^{\text{obs}}(\mathbf{x}_r)}{A(\mathbf{x}_r;\mathbf{m})}\right]^2, \tag{22}$$

where A represents the RMS amplitude of the synthetic seismogram in time window $\mathrm{w}(t) = [t_1, t_2]$

$$A(\mathbf{x}_r;\mathbf{m}) = \sqrt{\frac{1}{t_2 - t_1}\int_0^{t'}\left[\mathrm{w}(t)\,u_i(\mathbf{x}_r, t;\mathbf{m})\right]^2 dt}, \tag{23}$$

and A^{obs} is the RMS amplitude of the observed data. The regular adjoint source of the RMS-AR misfit function is derived as

$$f_{i,\text{RMS-AR}}^{\dagger}(\mathbf{x}, t) = -\sum_{\mathbf{x}_r}\ln\left[\frac{A^{\text{obs}}(\mathbf{x}_r)}{A_i(\mathbf{x}_r;\mathbf{m})}\right]\frac{\mathrm{w}(t)\,u_i(\mathbf{x}_r, t;\mathbf{m})}{(t_2 - t_1)\,A^2(\mathbf{x}_r;\mathbf{m})}\delta(\mathbf{x} - \mathbf{x}_r). \tag{24}$$

The adjoint source for calculating the attenuation sensitivity kernels can be obtained by inserting the Fourier transform of the adjoint source $f_{i,\text{RMS-AR}}^{\dagger}$ into equation (16).

Spectral amplitude-ratio misfit function

The SR method is widely used to estimate Q values, because the phase information is naturally separated from the amplitude information in the frequency domain. An associated spectral amplitude-ratio (S-AR) misfit function is defined in the frequency domain as:

$$\chi^{\text{S-AR}}(\mathbf{m}) = \frac{1}{2}\sum_{\mathbf{x}_r}\int_0^{\omega'}\left[\ln\frac{\mathcal{A}_i^{\text{obs}}(\mathbf{x}_r, \omega)}{\mathcal{A}_i(\mathbf{x}_r, \omega;\mathbf{m})}\right]^2 d\omega, \tag{25}$$

where ω' indicates the maximum angular frequency, $\mathcal{A}_i^{\text{obs}}$ and $\mathcal{A}_i$ are the amplitude spectrum of the observed and synthetic data within the frequency band of $\tilde{\mathrm{w}}(\omega)$. The regular adjoint source of the S-AR misfit function in frequency domain is given by

$$\tilde{f}_{i,\text{S-AR}}^{\dagger}(\mathbf{x}, \omega) = -\sum_{\mathbf{x}_r}\ln\left[\frac{\mathcal{A}_i^{\text{obs}}(\mathbf{x}_r, \omega)}{\mathcal{A}_i(\mathbf{x}_r, \omega;\mathbf{m})}\right]\frac{\tilde{\mathrm{w}}(\omega)\,u_i^{\ddagger}(\mathbf{x}_r, \omega;\mathbf{m})}{\mathcal{A}_i^2(\mathbf{x}_r, \omega;\mathbf{m})}\delta(\mathbf{x} - \mathbf{x}_r). \tag{26}$$

where $\ddagger$ denotes the complex conjugate. The time domain form of the adjoint source (used for calculating the attenuation sensitivity kernels) can be obtained by substituting equation (26) into equation (16).

DIFFERENT MODEL PARAMETERIZATIONS FOR ANISOTROPIC-ELASTIC FWI IN VTI MEDIA

When the seismic waves propagate in subsurface media, the traveltime at different directions are affected by the anisotropy effects a lot. Anisotropy also produces influences on the amplitudes of the seismic reflections. Thus, ignoring anisotropy effects in elastic FWI may produce distorted velocity estimations. Different model parameterizations in VTI media have different inversion performances for anisotropic-elastic FWI. In this report, we design four different model parameterizations including elastic-constant (c_{11}, c_{13}, c_{33} and c_{44}), velocity-Thomsen-I (α, β, ε and δ), velocity-Thomsen-II ($\alpha_h = \alpha\sqrt{1+2\varepsilon}$, β, ε and $\eta = \frac{\varepsilon-\delta}{1+2\delta}$) and VTI-velocity ($\alpha$, β, $\alpha_h = \alpha\sqrt{1+2\varepsilon}$, and $\alpha_{nmo} = \alpha\sqrt{1+2\delta}$).

Our inversion results show that in the model parameterizations of elastic-constant and VTI-velocity, incorporating anisotropy in elastic FWI produces the models with more continuous and coherent geological formations. In the model parameterizations of velocity-Thomsen-I and velocity-Thomsen-II, it is difficult to control the magnitudes of updates of the Thomsen parameters. Only very weak updates appear in the inverted models of Thomsen parameters. The improvements in inverted velocity models using velocity-Thomsen-I and velocity-Thomsen-II parameterizations are not obvious.

SENSITIVITY ANALYSIS FOR ATTENUATION ESTIMATION WITH DIFFERENT MISFIT FUNCTIONS

We begin with a sensitivity analysis carried out using a synthetic example; our summary here is designed to illustrate the advantages of the amplitude-based misfit functions for attenuation estimation in the presence of velocity errors. The numerical experiments in this study are carried out using the open-source software package SeisElastic2D based on the spectral-element forward modelling software package SPECFEM2D (Komatitsch and Tromp, 2005).

The model is 0.25 km wide and 0.5 km deep with 25 and 50 elements uniformly distributed in the X and Z directions. The unstructured quadrilateral spectral-element mesh is defined using 5 $\times$ 5 Gauss-Legendre-Lobatto points. A total of 20301 grid points are generated to characterize the model. The initial velocity and attenuation models are homogeneous with α = 2.0 km/s, β = 1.4 km/s and Q_α = Q_β = 100. The true α and β models are created by embedding velocity anomalies in the upper parts of the velocity models, as shown in Figures 1a-1b. To examine the influence of velocity errors on attenuation estimation, velocity anomalies with + 5 $\%$ and 10 $\%$ perturbations of the background values are applied, respectively. The true Q_α and Q_β models are created by embedding the attenuation anomalies (Q_α = Q_β = 10) in the lower parts of the attenuation models, as plotted in Figures 1c-1d. The influence of density on attenuation estimation is neglected in this paper. The true and initial ρ' models are homogeneous with a constant value of 1.5 kg/m^3. We arrange a total of 32 sources and 120 receivers on the left and right sides of the model, as indicated by the green triangles and red stars in Figure 1a. A P-SV mode source with a 30 Hz dominant frequency Ricker wavelet is used to generate the observed data.

We first calculate the attenuation sensitivity kernels using different misfit functions in

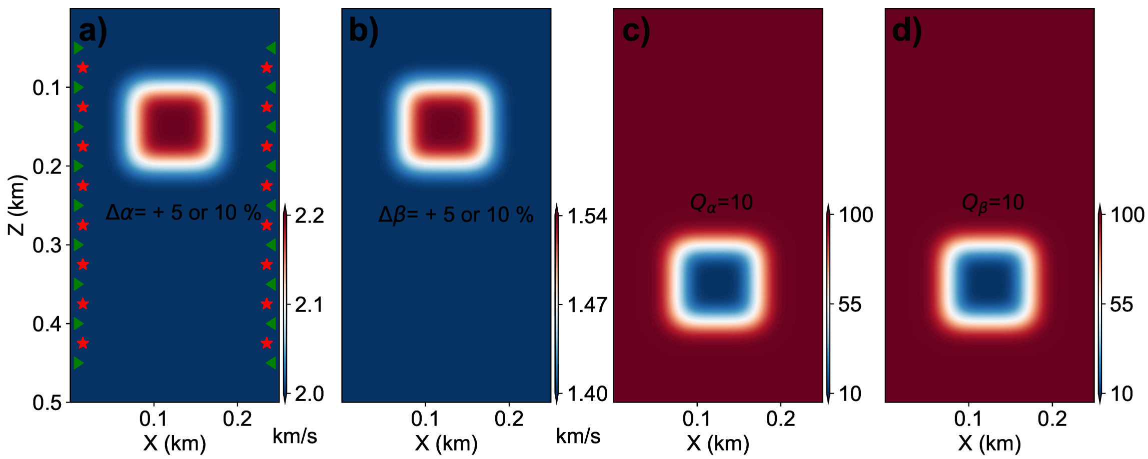

FIG. 1. (a) True α model; (b) True β model; (c) True Q_α model; (d) True Q_β model.

the presence of + 10 $\%$ velocity perturbations, as illustrated in Figure 2. The WD misfit function attenuation sensitivity kernels (Figures 2a-2b) are strongly contaminated by the velocity errors artifacts (gray arrows), which are much stronger than the correct attenuation updates (black arrows). When using the I-AR misfit function, the correct attenuation updates (black arrows in Figures 2c-2d) appear to be relative stronger, compared to the WD misfit function attenuation sensitivity kernels. However, the parameter crosstalks are still very strong, as indicated by the gray arrows in Figures 2c-2d. In the attenuation sensitivity kernels calculated using the RMS-AR and S-AR misfit functions (Figures 2e-2h), the correct attenuation updates become stronger than the parameter crosstalks. We then calculate the attenuation sensitivity kernels using different misfit functions with + 5 $\%$ velocity perturbations, as illustrated in Figure 3. Compared to Figure 2, the parameter crosstalks in the attenuation sensitivity kernels calculated by the amplitude-based misfit functions are much weaker. However, the WD misfit function attenuation sensitivity kernels still exhibit very strong parameter crosstalks.

Next, we carry out experiments to invert for the attenuation models in the presence of + 5 $\%$ velocity perturbations. In Figure 4 the attenuation models determined from the different misfit functions are plotted. We observe that, because of strong parameter crosstalks, the WD misfit function only inverts weak attenuation anomalies ($Q_\alpha \approx 92$ and $Q_\beta \approx 88$), as indicated by the black arrows in Figures 4a-4b. The WD data misfit also reduces slightly, by 8$\%$, after 3 iterations. Figures 4c-4h show the attenuation models determined through minimization of the amplitude-based misfit functions. The I-AR, RMS-AR and S-AR data misfits reduces by approximately 27.7 $\%$, 69.8 $\%$ and 69.7 $\%$ after 5, 7 and 6 iterations, respectively. Furthermore, stronger attenuation anomalies ($Q_\alpha \approx 38$ and $Q_\beta \approx 14$) are resolved in the inverted attenuation models.

These observations in the synthetic inversion experiments suggest that, in comparison to the standard WD misfit function, the amplitude-based misfit functions respond sharply to attenuation anomalies and appear to produce a higher degree of accuracy in attenuation models in the presence of velocity errors.

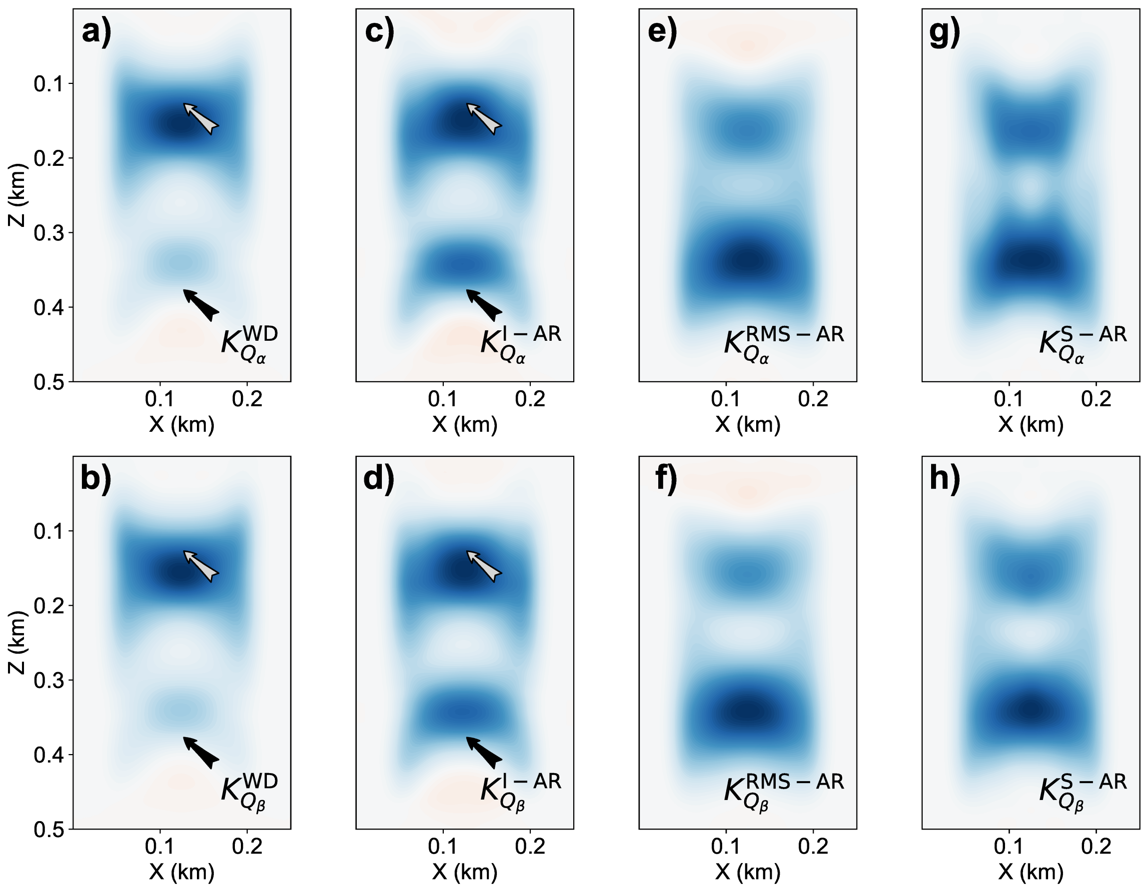

FIG. 2. Attenuation sensitivity kernels calculated using different misfit functions in the presence of + 10 $\%$ velocity perturbations. (a-b) are the WD misfit function attenuation sensitivity kernels $K_{Q_\alpha}^{\text{WD}}$ and $K_{Q_\beta}^{\text{WD}}$;(c-d) are the I-AR misfit function attenuation sensitivity kernels $K_{Q_\alpha}^{\text{I-AR}}$ and $K_{Q_\beta}^{\text{I-AR}}$; (e-f) are the RMS-AR misfit function attenuation sensitivity kernels $K_{Q_\alpha}^{\text{RMS-AR}}$ and $K_{Q_\beta}^{\text{RMS-AR}}$;(g-h) are the the S-AR misfit function attenuation sensitivity kernels $K_{Q_\alpha}^{\text{S-AR}}$ and $K_{Q_\beta}^{\text{S-AR}}$. The blue color indicates positive value.

FIELD W-VSP DATASET APPLICATION

We next apply viscoelastic FWI to the practical W-VSP dataset for attenuative reservoir characterization with the two-stage inversion strategy and amplitude-based misfit functions.

Geological background and data preparation

The W-VSP survey was carried out in a producing heavy-oil field of Western Canada in 2011. The VectorSeis accelerometers were arranged from depth 70 m to 512 m with a regular interval of 2 m in the borehole. Both dynamite sources (0.125 kg charge) and EnviroVibe sources (10-300 Hz linear sweep over 20 s) were used for data acquisition. The maximum recording time is 3 s with a sampling interval of 0.001 s. In Figure 5 the acquisition configuration of the W-VSP survey is illustrated.

The target formation in the study area is one stratigraphical unit of Cretaceous age in the Western Canadian Sedimentary Basin; it was deposited as prograding tide-dominated

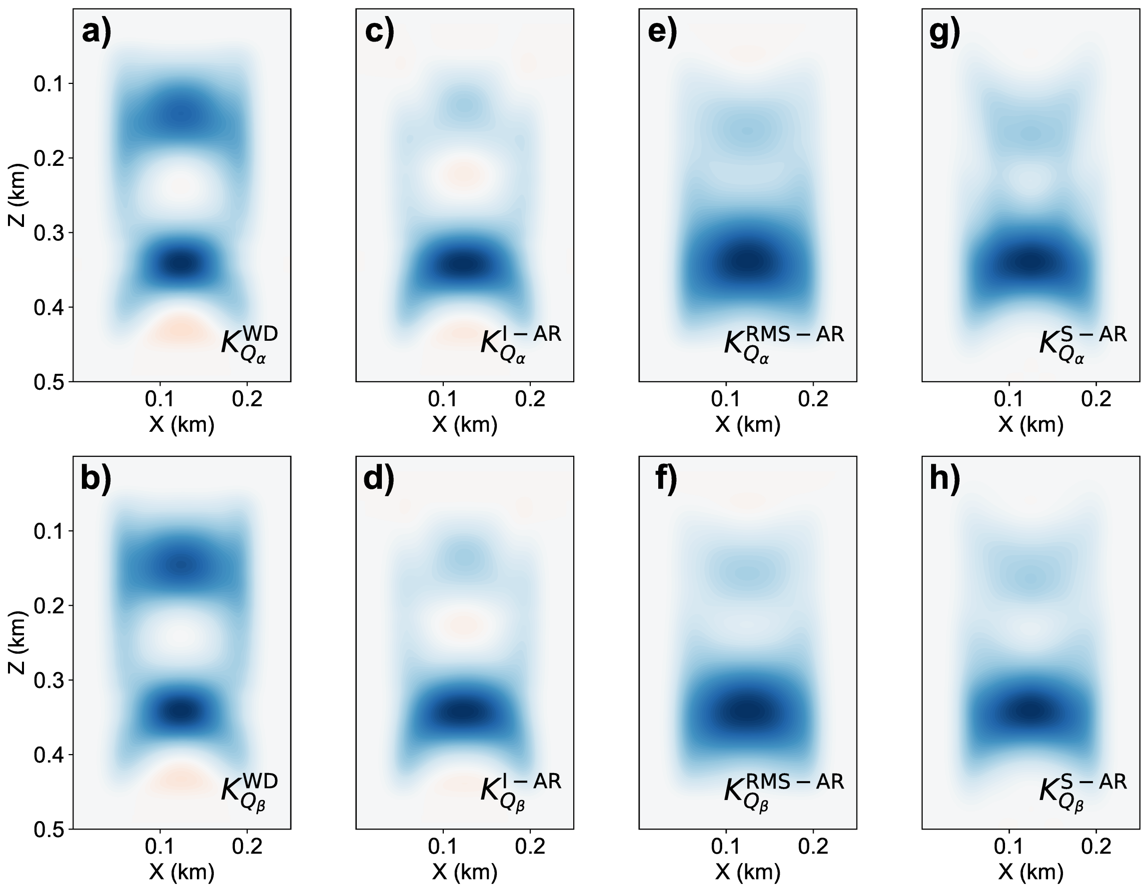

FIG. 3. The corresponding attenuation sensitivity kernels calculated using different misfit functions in the presence of + 5 $\%$ velocity perturbations.

deltas and is composed of stacked incised valleys that lie encased within more regional deltaic, shoreface sands and marine muds. In Figures 6a-6c, we plot the α, ρ' and Gamma ray well-logs from the borehole. In Figure 6a, the Clearwater formation (depth $\sim$ 0.45-0.5 km), conformably overlain by the Grand Rapids formation and overlies the McMurray formation within the Mannville Group, displays low α, ρ' and Gamma ray values, indicating potential hydrocarbon deposits. We calculate the β well-log (Figure 6e) from the α/β ratio log (Figure 6d) obtained from an adjacent well. The α/β ratio, an important lithology discriminator, will contain inaccuracies because of the distance between the two wells, but it provides a plausible source for an approximate β log.

The EnviroVibe source W-VSP data with a known Klauder source wavelet is used for viscoelastic FWI. Figures 7a-7b show the Klauder source wavelet and its amplitude spectrum. We apply a series of operations to pre-process the EnviroVibe source W-VSP data. Traces with abnormal amplitudes and polarities are removed. Horizontal component rotation is applied using the principal component analysis method. Topographic variations are compensated for with elevation statics. We select 6 shot gathers with which to perform the inversion, focusing on the area around the borehole. The source and receiver locations after re-datuming are illustrated in Figure 5. Figures 8a-8c show the processed vertical (z) and radial (x) component shots at horizontal position of 0.09 km within the time window of 0-0.8 s. We observe strong direct down-going P- and S-waves radiating from the source.

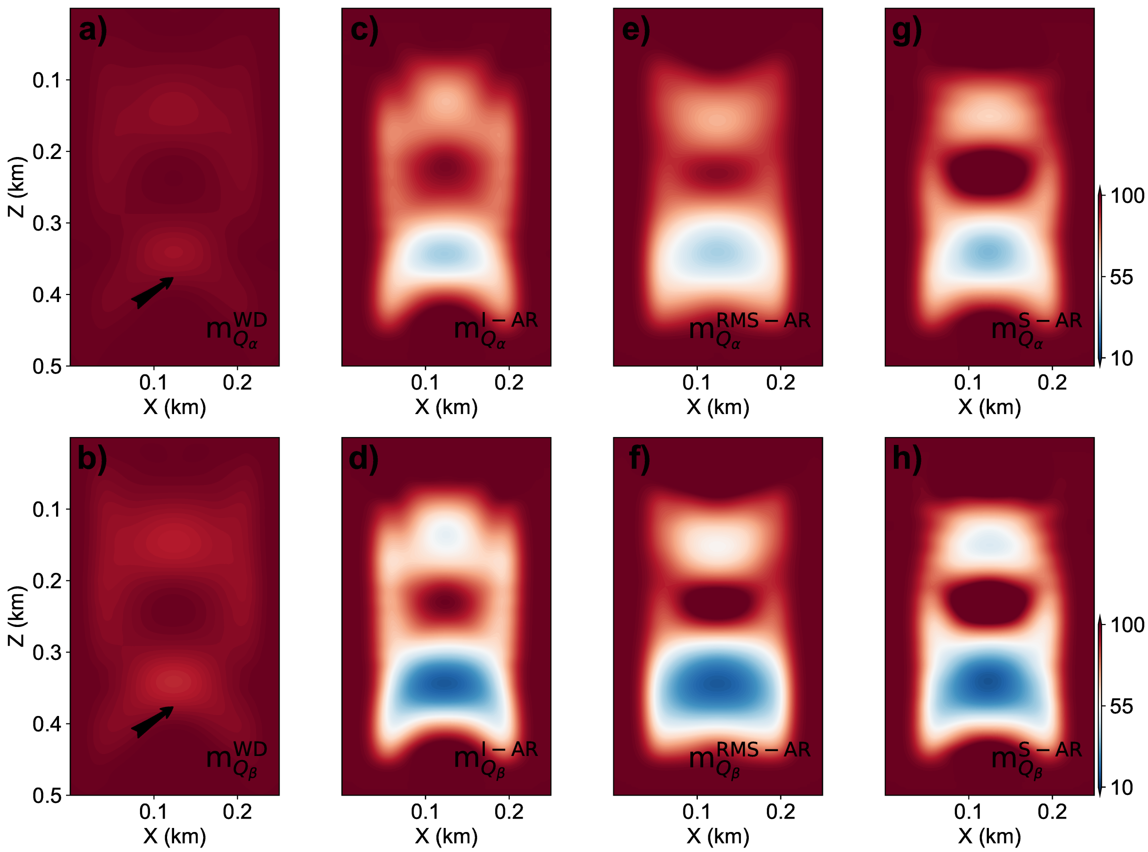

FIG. 4. The inverted attenuation models obtained using different misfit functions in the presence of + 5 % velocity perturbations. (a-b) are the WD misfit function inverted attenuation models $\mathbf{m}_{Q_\alpha}^{\text{WD}}$ and $\mathbf{m}_{Q_\beta}^{\text{WD}}$. (c-d) are the I-AR misfit function inverted attenuation models $\mathbf{m}_{Q_\alpha}^{\text{I-AR}}$ and $\mathbf{m}_{Q_\beta}^{\text{I-AR}}$; (e-f) are the RMS-AR misfit function inverted attenuation models $\mathbf{m}_{Q_\alpha}^{\text{RMS-AR}}$ and $\mathbf{m}_{Q_\beta}^{\text{RMS-AR}}$; (a-b) are the S-AR misfit function inverted attenuation models $\mathbf{m}_{Q_\alpha}^{\text{S-AR}}$ and $\mathbf{m}_{Q_\beta}^{\text{S-AR}}$.

Reflected up-going P-waves in the z component and converted down-going and up-going S-waves in the x component can also be identified clearly.

In Figure 9, we plot the amplitude spectrum of the direct down-going P-waves (time window Tb) and down-going S-waves (time window Ta) in the z and x component shots. High frequencies within the down-going P-waves (100-200 Hz) and the down-going S-waves (30-60 Hz) are observed to decrease significantly; this is attributable to seismic attenuation. For the down-going P-waves (Figures 9a-9b), from trace 50 to 150 (depth $\sim$ 0.17-0.37 km), magnitudes of the amplitude spectrum reduce significantly, indicating strong P-wave attenuation within this zone. For the down-going S-waves (Figures 9c-9d), magnitudes of the amplitude spectrum decrease from trace 40 to 100 (depth $\sim$ 0.15-0.27 km), indicating strong S-wave attenuation within this zone. Partial amplitude reduction is also attributed to geometrical spreading, reflection and transmission loss, etc.

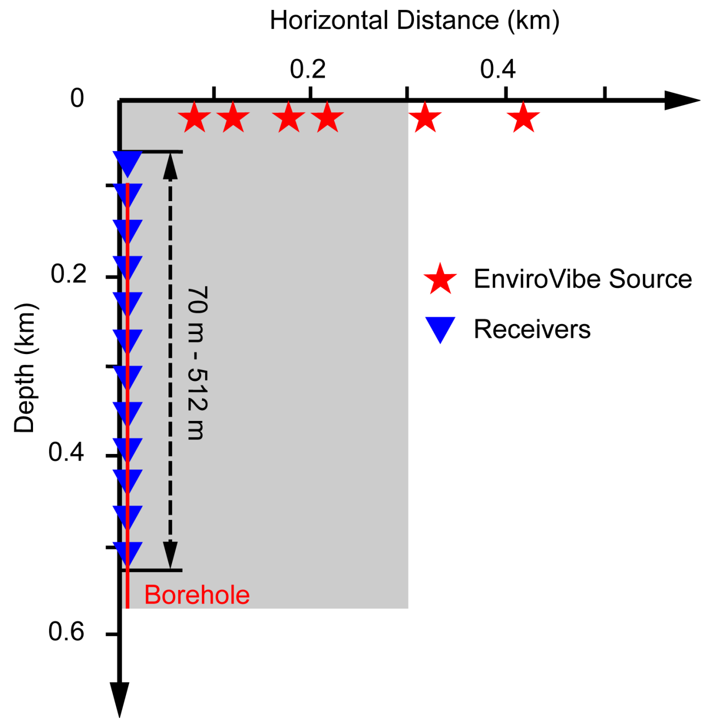

FIG. 5. The W-VSP acquisition configuration. The red stars and blue triangulares indicate the positions of the EnviroVibe sources and receivers. The red line indicates the location of the borehole at horizontal distance of 0.01 km.

Building initial models and inversion strategy

The 1D initial α and β models (Figures 10a-10b) are created by smoothing the well-log data. The model is 0.57 km deep and 0.54 km wide, with 108 and 100 elements uniformly distributed in vertical and horizontal dimensions. A total of 173633 grid points are produced to characterize the model. The derived initial α/β ratio model is shown in Figure 10c. From our previous studies, the lateral ρ' variation is small. Thus, the ρ' model is created by slightly smoothing the well-log data and kept unchanged in the inversion experiment. We first estimate the Q_α and Q_β models using the traditional SR and CFS methods and then use the averaged Q_α and Q_β values to create the initial attenuation models for viscoelastic FWI, as shown in Figures 10e-10f.

As we observed in the synthetics, velocity errors can produce strong parameter crosstalk artifacts in the inverted attenuation models. However, the influence of attenuation on velocity estimation is less significant (Kamei and Pratt, 2013; Fabien-Ouellet et al., 2017). Thus, a two-stage inversion strategy is designed and carried out for this viscoelastic FWI problem. We designed time windows Ta and Tb (red and blue shaded areas in Figure 8a) to separate the direct down-going S-waves and P-waves radiating from the source. This is designed to reduce potentially damaging tradeoffs between the source mechanism and structure models. In stage-I, we invert β model in time window Ta and then invert α and β models simultaneously in time window Tb using the standard WD misfit function. A multi-scale strategy is applied by expanding the frequency band from [12 Hz, 30 Hz] to [12 Hz, 60 Hz]. At each frequency band, we terminate the inversion when the data misfit reduces to sufficiently small value. In stage-II, we invert the Q_β model using the direct

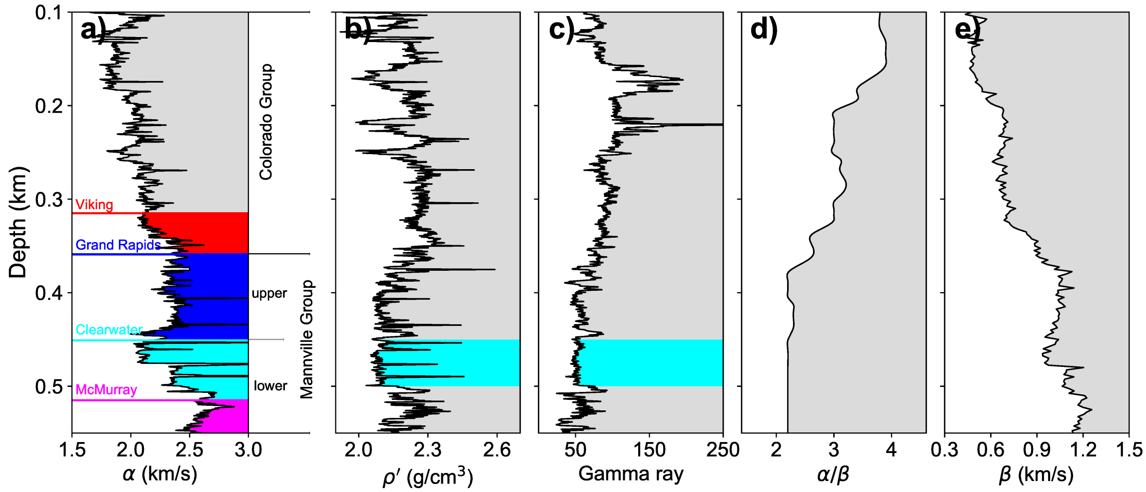

FIG. 6. (a-e) are the well-log data of α, ρ', Gamma ray, α/β ratio and β. In (a), the red shaded area indicates the Viking formation (lower Colorado Group). The blue shaded area indicates the Grand Rapids formation (upper Mannville Group). The cyan and magenta shaded areas are the Clearwater and McMurray formations forming the lower Mannville Group.

down-going S-waves in time window Ta. In time window Tb, we use a median filter to separate P- and S-waves, which are then used to invert the Q_α and Q_β models. The three amplitude-based misfit functions are applied to invert the Q_α and Q_β models compared to the WD misfit function.

Stage-I inversion results

In the stage-I inversion experiment, we obtain high-resolution α and β models, as shown in Figures 11a-11b. The WD data misfit reduces by approximately 83.0% after a total of 67 iterations. Due to source-receiver illumination limitations, we only plot the inverted models with a maximum horizontal distance of 0.3 km, as indicated by the gray area in Figure 5. Trend variations of the α model match the well-log data closely. The low α anomaly in the Clearwater formation (depth $\sim$ 0.45-0.5 km) has been successfully determined, as indicated by the arrow and cyan-shaded area in Figure 11a. The derived α/β ratio and Poisson's ratio models are shown in Figures 11c-11d. Because the sandstones saturated with heavy-oil resources have lower α/β ratios than the shale formations, the α/β ratio is always used to map the subsurface bitumen sands. From the Grand Rapids formation to the target Clearwater formation, the α/β ratio derived from the waveform data reduces from 2.2 to 1.6 and the Poisson's ratio drops from 0.36 to 0.23. This is associated with the lithology change from shale to sand, as indicated by the arrows and cyan-shaded areas in Figures 11c-11d.

In Figures 12a-12d the z and x component observed data are compared with the synthetic data calculated from the initial models. In time windows Tb and Ta, the traveltime and phase differences of the down-going P- and S-waves between the observed and synthetic data can be observed, as indicated by the red and blue ellipses. Amplitudes of the down-going P- and S-waves in the synthetic data are much stronger than those of the observed data, as indicated by the cyan and red arrows. The amplitude spectra of the synthetic

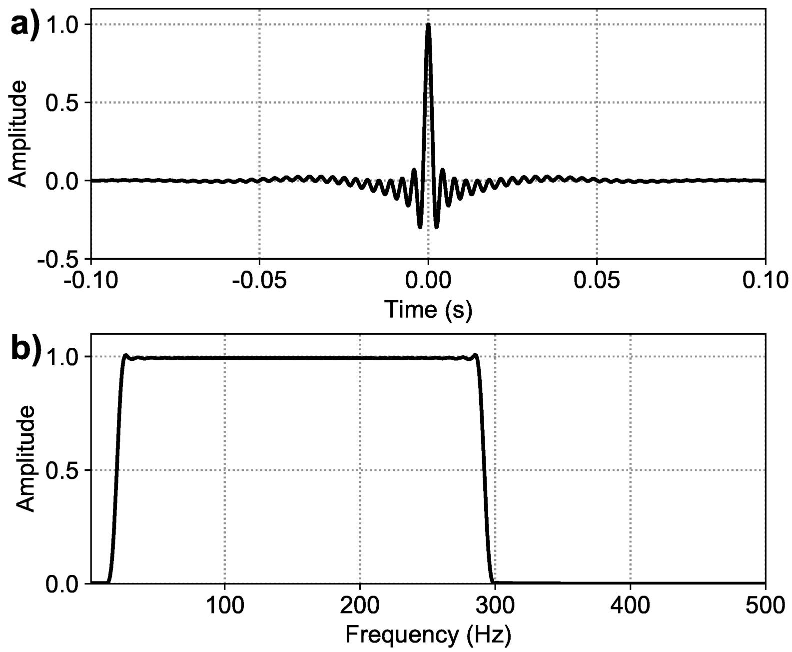

FIG. 7. (a) is the zero phase Klauder source wavelet; (b) is the amplitude spectrum of the source wavelet.

data and the observed data are plotted in Figure 13; large differences between the two are observed. From trace 50 to 150, the amplitude spectra of the observed data are for instance observed to be much weaker than those of the synthetic data calculated from the initial models.

In Figures 12e-12h the observed data and the synthetic data calculated from the stage-I inverted models are compared. The traveltime of the down-going P- and S-waves of the synthetic data match those of the observed data well, suggesting that the inverted α and β models are capturing much of true velocity information in the medium. Converted down-going and up-going S-waves in x component of the synthetic data (Figure 12f) can be identified clearly. In Figure 14, the differences between the stage-I synthetic amplitude spectra and those of the observed data are much weaker than the amplitude spectrum differences in Figure 13. We attribute this to the amplitude reduction caused by reflection and transmission processes rather than seismic intrinsic attenuation. Although the initial Q_α and Q_β models are considered for the forward modeling, we observe that the amplitudes of the down-going P- and S-waves of the stage-I synthetic data are still stronger than those of the observed data, as indicated by the red and cyan arrows in Figure 12. Furthermore, the amplitude spectra of the stage-I synthetic data are still stronger than those of the observed data, especially from trace 50 to 150, as indicated by the red dash squares in Figures 13 and 14. We attribute this component of the amplitude loss to attenuation; actual Q_α and Q_β values are expected to be lower in this region of the model.

Estimating attenuation models using amplitude-based misfit functions in stage-II

Even though the velocity models in stage-I have been improved significantly, the residual velocity errors may still produce parameter crosstalk artifacts in the inverted attenuation

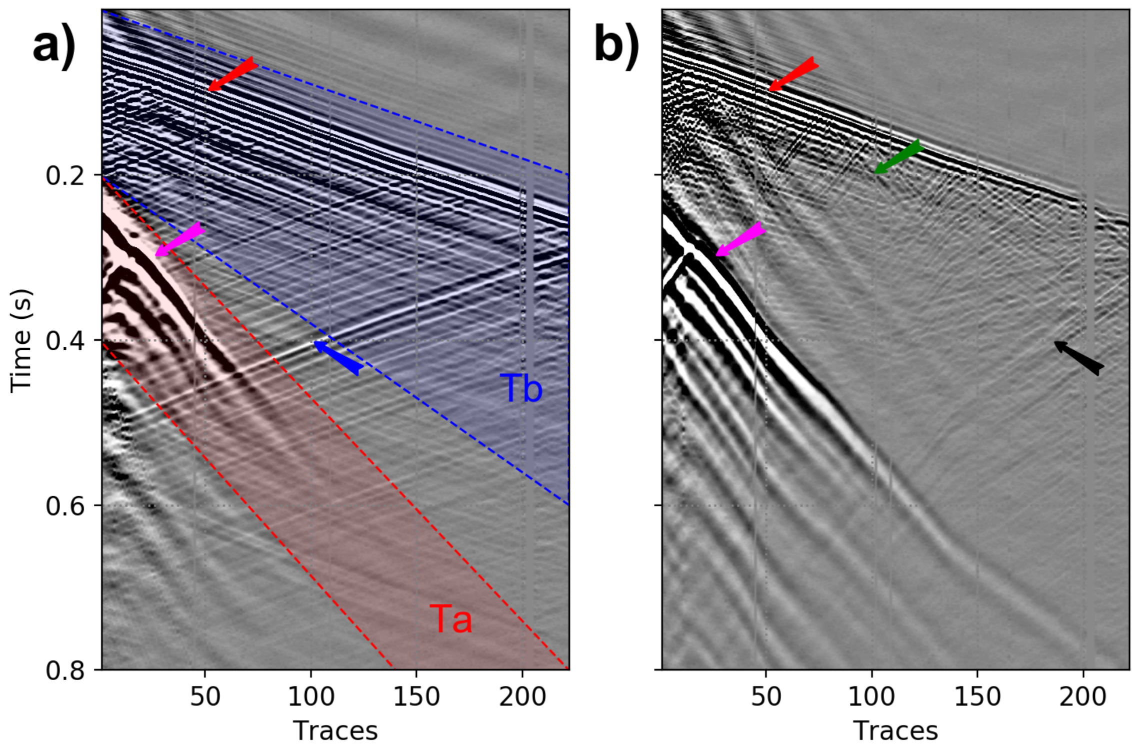

FIG. 8. (a-b) are the processed z and x component shots at horizontal location of 0.09 km. The red and blue shaded areas in (a) indicate the time windows Ta and Tb. The red and cyan arrows indicate the direct down-going P- and S-waves radiating from the source. The blue, green and black arrows indicate the reflected P-waves, converted down-going and up-going S-waves, respectively.

models. In the stage-II inversion experiment, we use the different amplitude-based misfit functions to estimate the Q_α and Q_β models compared to the traditional WD misfit function. In Figure 15 the inverted Q_α and Q_β models using the WD and I-AR misfit functions are plotted. The WD and I-AR data misfits reduce by approximately 15.2$\%$ and 35.6$\%$ after 56 and 43 iterations respectively. In Figure 16 the inverted Q_α and Q_β models using the RMS-AR and S-AR misfit functions are plotted. The RMS-AR and S-AR data misfits reduce by approximately 55.6$\%$ and 54.1$\%$ after 26 and 24 iterations respectively. In Figures 17 and 18 the observed data and the synthetic data calculated from the inverted attenuation models using the different misfit functions are plotted.

Compared to the initial attenuation models, the inverted Q_α and Q_β values as determined by minimizing the WD misfit function decrease by approximately 20-35 and 5-10 respectively. The anomaly at 0.45-0.5 km depth in the Q_α model is clearly identifiable. The I-AR misfit function inverts the attenuation models more efficiently than the WD misfit function and is associated with a decrease in the attenuation values around the borehole. Strong Q_α and Q_β anomalies are resolved at 0.45-0.5 km depth. Compared to the WD and I-AR misfit functions, the RMS-AR and S-AR misfit functions invert the attenuation models more efficiently and provide stronger attenuation anomalies at depths of 0.15-0.35 km and 0.45-0.5 km. The amplitudes of the synthetic down-going P- and S-waves decrease rapidly, and comparably to those in the observed data, as shown in Figure 18. The RMS-AR and S-AR misfit functions exhibit similar inversion performance, and provide attenuation

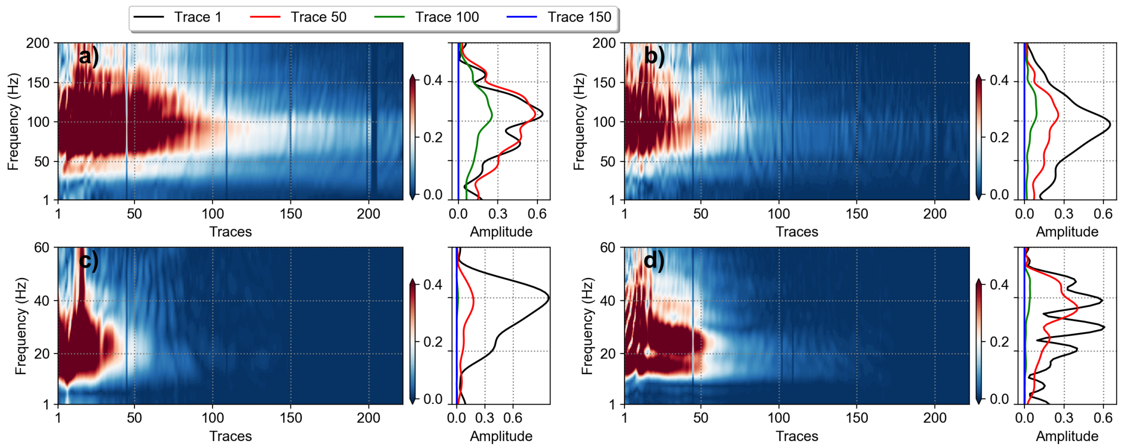

FIG. 9. (a-b) are the amplitude spectrum of the direct down-going P-waves of z and x component data (time window Tb); (c-d) are the amplitude spectrum of the direct down-going S-waves of z and x component data (time window Ta).

models of comparable quality.

We select the inverted Q_α and Q_β models by the RMS-AR misfit function (Figures 16a-16b) as the stage-II inverted attenuation models. Trends within the inverted Q_α and Q_β models are generally consistent with those of the α and β models. At 0.1-0.15 km in depth, relatively large Q_α and Q_β values are obtained, as are relatively large α and β values, as indicated by the arrows in Figure 11. At 0.17-0.35 km in depth, the relatively low Q_α ($\sim$ 20-30) and Q_β ($\sim$ 10-20) values are derived, which explain the significant amplitude losses of the traces 50-150 in the data. Higher Q_α ($\sim$ 30-45) and Q_β ($\sim$ 30-40) values are obtained at depth of 0.35-0.45 km, i.e., within the Grand Rapids formation shales. At depth of 0.45-0.5 km, lower Q_α ($\sim$ 25) and Q_β ($\sim$ 20) values are recovered within the heavy oil saturated Clearwater formation sandstones.

The amplitude spectra of the stage-II synthetic data are closer to those of the observed data and their differences become weaker, as shown in Figure 19. In Figure 20, traces 70 and 180 with their down-going S-waves and P-waves in the time windows Ta and Tb, and their amplitude spectra, are plotted in detail. Compared to the initial synthetic data (gray lines), the travel times of the stage-I synthetic data (blue lines) match those of the observed data (black lines) qualitatively closely, but still have much stronger amplitudes. However, both the amplitudes and traveltimes of the stage-II synthetic data exhibit a close match to those of the observed data. The amplitude spectra of the traces in stage-II synthetic data also exhibit an improved match with those of the observed data traces. Note that in the low frequency band (with band pass filtering), the central-frequency shift in the amplitude spectra caused by seismic attenuation is not obvious. For these reasons we consider the Q_α and Q_β models determined via the RMS-AR misfit function in stage-II to be the most compelling and plausible.

APPLYING ANISOTROPIC-ELASTIC FWI WITH DIFFERENT MODEL PARAMERTIZATIONS TO THE W-VSP DATA

In this section, we applied anisotropic-elastic FWI in VTI media with different model paramertizations to the W-VSP data. The model parameters in elastic-constant and VTI-velocity model parameterizations have the same physical units. Thus, the model parameters in these two model parameterizations are simultaneously inverted. The model parameters in velocity-Thomsen-I and velocity-Thomsen-I have different physical units. Thus, for these two model parameterizations, in stage-I, we invert the velocity parameters and Thomsen parameters simultaneously. The inverted Thomsen parameters have weak magnitudes. In stage-II, we only invert the Thomsen parameters.

The inverted models using the model parameterizations of elastic-constant, VTI-velocity, velocity-Thomsen-I, and velocity-Thomsen-II are given in Figures 21-24. Because we only use the frequency band of [12 Hz, 30 Hz] for inversion, the inverted models associated with S-wave velocity have lower resolution. AS can be seen that, the inverted models of c_{33} (Figure 21c) and α (Figure 22a) by the elastic-constant and VTI-velocity model parameterizations have very continuous and coherent geology formations. This is caused by the fact that in the inversion experiments the anisotropic models are reasonably updated. The geological formations in the inverted velocity models α and α_h (Figures 23a and 24a) by the velocity-Thmosen parameterizations appear to be distorted. This is because in the inversion process, the Thomsen parameters are not reasonably updated.

DISCUSSION

In the W-VSP data studied in this paper, the effects of high frequencies reduction ($\sim$ 100-200 Hz) and amplitude loss due to seismic attenuation are clearly discernible. Both the amplitude-based and central-frequency shift (Dutta and Schuster, 2016) misfit functions are potential candidates for attenuation estimation in viscoelastic FWI. However, in this study, the highest frequency used for inversion is 60 Hz. When using low frequency bands for inversion with the multi-scale strategy, the central-frequency difference between the synthetic and observed data, especially early in the process, is small and difficult to detect. Thus, the amplitude-based misfit functions are selected to invert the attenuation models for the W-VSP data. Amplitudes of the seismic data are also influenced by other factors including geometrical spreading, reflection and transmission loss, etc. The influence of geometrical spreading can be suppressed in the misfit function between the synthetic and observed data. Further, after the stage-I inversion step, we assume that more accurate P-wave velocity, S-wave velocity and density models have been obtained. Thus, the influence of reflection and transmission loss is also in principle removed, preparing the way for the attenuation inversion in stage-II using the amplitude-based misfit functions. Seismic attenuation also results in phase changes of the seismic data, but we proceed assuming these are much weaker than the phase changes caused by velocity perturbations. When this is true, strong velocity-attenuation tradeoffs should be expected when using a phase misfit function for attenuation estimation.

In the paper of Pan et al. (2018b), we evaluated the performances of different model parameterizations for isotropic-elastic FWI without considering attenuation using the dynamite source W-VSP data. However, errors in the estimated dynamite source wavelet exposed us to potential biased velocity estimations due to the source-structure tradeoffs. In this study, we apply viscoelastic FWI to EnviroVibe source data, with the known Klauder source wavelet. Although the low-frequency content and energy of the EnviroVibe data will tend to be weaker than those associated with dynamite source, because of better source control, we should be less exposed to damaging tradeoffs between the source time function and the structure models. The strong S-waves contained in the EnviroVibe source data also lead to more stable, and presumably accurate, S-wave velocity model. The attenuation models derived from FWI lead to a significant improvement in match between the synthetic and observed data, and provide independent constraints on the rock properties for lithology discrimination and reservoir characterization.

When simultaneously inverting seismic data for velocity and attenuation parameters, strong parameter crosstalks tend to appear in the recovered attenuation models. In this study, a two-stage inversion strategy is employed, in which the velocity and attenuation parameters are determined sequentially. Further detailed comparisons between the sequential and simultaneous inversion strategies are under way and will be reported on in a future communication.

W-VSP data, with their strong transmission modes and relatively complete ray path coverage, are in many ways ideal for analyses of multiparameter elastic FWI and related workflows. Here we make use of a high quality dataset of this kind to analyze the relative merits of various amplitude-based misfit functions. Performances and stability of these amplitude-based misfit functions should be evaluated using reflection seismic data. The adjoint sources for calculating the attenuation sensitivity kernels are derived based on the assumption that the quality factor Q is constant within the seismic frequency band, which also increases the computational cost. Frequency-dependent (or independent) attenuation sensitivity kernels can be calculated following Fichtner and van Driel (2014).

CONCLUSION

Visocoelastic FWI is applied to practical W-VSP data acquired at a producing heavy-oil field in Western Canada for attenuative reservoir characterization. To reduce the strong velocity-attenuation tradeoffs, a two-stage inversion strategy is designed and carried out. The amplitude-based misfit functions show stronger sensitivity to attenuation anomalies in the presence of velocity errors and then are used to invert the attenuation models in stage-II. Overall, the RMS-AR and S-AR misfit functions invert the attenuation models more reliably than the other misfit function choices. In the final inversion results, obvious reductions of α/β ratio and Poisson's ratio models within the Clearwater formation clearly indicate the occurrence of the heavy-oil resources. Strong Q_α and Q_β anomalies in this zone also provide independent constraints on the rock properties for identifying the attenuative reservoir. The performances of different model parameterizations in anisotropic-elastic FWI are evaluated.

ACKNOWLEDGMENTS

This research was partially supported by the Consortium for Research in Elastic Wave Exploration Seismology (CREWES) and National Science and Engineering Research Council of Canada (NSERC, CRDPJ 461179-13), and in part from the Canada First Research Excellence Fund. Thanks High Definition Seismic Corporation for providing the Vector-Seis phones. WP was supported by SEG/Chevron Scholarship and Eyes High International Doctoral Scholarship. The Tiger cluster (Princeton University) is acknowledged for providing parallel computing support.

REFERENCES

Aki, K., and Richards, P. G., 2002, Quantitative Seismology: University Science Books.

Alkhalifah, T., and Plessix, R., 2014, A recipe for practical full-waveform inversion in anisotropic media: An analytic parameter resolution study: Geophysics, **79**, R91–R101.

Bai, T., Tsvankin, I., and Wu, X., 2017, Waveform inversion for attenuation estimation in anisotropic media: Geophysics, **82**, WA83–WA93.

Bath, M., 1974, Spectral analysis in geophysics: Developments in Solid Earth Geophysics: Elsevier Science Publishing Co.

Blanch, J. O., Robertsson, J. O. A., and Symes, W. W., 1995, Modeling of a constant Q: Methodology and algorithm for an efficient and optimally inexpensive viscoelastic technique: Geophysics, **60**, 176–184.

Bozdağ, E., Peter, D., Lefebvre, M., Komatitsch, D., Tromp, J., Hill, J., Podhorszki, N., and Pugmire, D., 2016, Global adjoint tomography: first-generation model: Geophysical Journal International, **207**, 1739–1766.

Bozdağ, E., Trampert, J., and Tromp, J., 2011, Misfit functions for full waveform inversion based on instantaneous phase and envelope measurements: Geophysical Journal International, **185**, 845–870.

Brossier, R., 2011, Two-dimensional frequency-domain visco-elastic full waveform inversion: Parallel algorithms, optimization and performance: Computer & Geosciences, **37**, 444–445.

Brossier, R., Operto, S., and Virieux, J., 2009, Seismic imaging of complex onshore structures by 2D elastic frequency-domain full-waveform inversion: Geophysics, **74**, WCC105–WCC118.

Carcione, J. M., Kosloff, D., and Kosloff, R., 1988a, Viscoacoustic wave propagation simulation in the earth: Geophysics, **53**, 769–777.

Carcione, J. M., Kosloff, D., and Kosloff, R., 1988b, Wave propagation simulation in a linear viscoacoustic medium: Geophysical Journal International, **93**, 393–407.

Chen, H., and Innanen, K. A., 2018, Estimating P- and S-wave inverse quality factors from observed seismic data using an attenuative elastic impedance: Geophysics, **83**, R173–R187.

Chen, K., and Sacchi, M. D., 2018, The importance of including density in elastic least-squares reverse time migration: multiparameter crosstalk and convergence: Geophysical Journal International.

Dahlen, F. A., and Baig, A. M., 2002, Fréchet kernels for body-wave amplitudes: Geophysical Journal International, **150**, 440–466.

Dahlen, F. A., and Tromp, J., 1998, Theoretical Global Seismology: Princeton University Press.

Dutta, G., and Schuster, G. T., 2014, Attenuation compensation for least-squares reverse time migration using the viscoacoustic-wave equation: Geophysics, **79**, S251–S262.

Dutta, G., and Schuster, G. T., 2016, Wave-equation *Q* tomography: Geophysics, **81**, R471–R484.

Fabien-Ouellet, G., Gloaguen, E., and Giroux, B., 2017, Time domain viscoelastic full waveform inversion: Geophysical Journal International, **209**, 1718–1734.

Fichtner, A., and van Driel, M., 2014, Models and Fréchet kernels for frequency-(in)dependent *Q*: Geophysical Journal International, **198**, 1878–1889.

Guitton, A., and Díaz, E., 2012, Attenuating crosstalk noise with simultaneous source full waveform inversion: Geophysical Prospecting, **60**, 759–768.

Guo, P., and McMechan, G. A., 2018, Compensating *Q* effects in viscoelastic media by adjoint-based least-squares reverse time migration: Geophysics, **83**, S151–S172.

Guo, P., McMechan, G. A., and Guan, H., 2016, Comparison of two viscoacoustic propagators for *Q*-compensated reverse time migration: Geophysics, **81**, S281–S297.

Innanen, K. A., 2011, Inversion of the seismic AVF/AVA signatures of highly attenuative targets: Geophysics, **76**, R1–R14.

Innanen, K. A., 2014, Seismic AVO and the inverse Hessian in precritical reflection full waveform inversion: Geophysical Journal International, **199**, 717–734.

Innanen, K. A., and Lira, J. E., 2010, Direct nonlinear *Q*-compensation of seismic primaries reflecting from a stratified, two-parameter absorptive medium: Geophysics, **75**, V13–V23.

Kamei, R., and Pratt, R. G., 2013, Inversion strategies for visco-acoustic waveform inversion: Geophysical Journal International, **194**, 859–884.

Keating, S., and Innanen, K. A., 2018, Parameter cross-talk and modelling errors in viscoacoustic seismic full waveform inversion: Geophysics, submitted.

Komatitsch, D., and Tromp, J., 2005, Introduction to the spectral-element method for 3-D seismic wave propagation: Geophysical Journal Interational, **139**, 806–822.

Leeuwen, T. V., and Mulder, W. A., 2010, A correlation-based misfit criterion for wave-equation traveltime tomography: Geophysical Journal International, **3**, 1383–1394.

Liu, H., Anderson, D. L., and Kanamori, H., 1976, Velocity dispersion due to anelasticity; implications for seismology and mantle composition: Geophysical Journal International, **47**, 41–58.

Liu, Q., and Tromp, J., 2006, Finite-frequency kernels based on adjoint methods: Bulletin of the Seismological Society of America, **96**, 2383–2397.

Liu, Q., and Tromp, J., 2008, Finite-frequency sensitivity kernels for global seismic wave propagation based upon adjoint methods: Geophysical Journal International, **174**, 265–286.

Margrave, G. F., Lamoureux, M. P., and Henley, D. C., 2011, Garbor deconvolution: Estimating reflectivity by nonstationary deconvolution of seismic data: Geophysics, **76**, W15–W30.

Métivier, L., Brossier, R., Operto, S., and Virieux, J., 2015, Acoustic multi-parameter FWI for the reconstruction of P-wave velocity, density and attenuation: preconditioned truncated Newton approach: SEG Expanded Abstracts, 1198–1203.

Moradi, S., and Innanen, K. A., 2015, Scattering of homogeneous and inhomogeneous seismic waves in low-loss viscoelastic media: Geophysical Journal International, **202**, 1722–1732.

Nocedal, J., and Wright, S. J., 2006, Numerical Optimization: Springer.

Operto, S., Gholami, Y., Prieux, V., Ribodetti, A., Brossier, R., Metivier, L., and Virieux, J., 2013, A guided tour of multiparameter full waveform inversion with multicomponent data: from theory to practice: The Leading Edge, **32**, 1040–1054.

Operto, S., and Miniussi, A., 2018, On the role of density and attenuation in 3D multi-parameter visco-acoustic VTI frequency-domain FWI: an OBC case study from the North Sea: Geophysical Journal International, **213**, 2037–2059.

Pan, W., Geng, Y., and Innanen, K. A., 2018a, Interparameter tradeoff quantification and reduction in isotropic-elastic full-waveform inversion: synthetic experiments and Hussar land data set application: Geophysical Journal International, **213**, 1305–1333.

Pan, W., Innanen, K. A., and Geng, Y., 2018b, Elastic full-waveform inversion and parameterization analysis applied to walk-away vertical seismic profile data for unconventional (heavy oil) reservoir characterization: Geophysical Journal International, **213**, 1934–1968.

Pan, W., Innanen, K. A., Geng, Y., and Li, J., 2019, Interparameter tradeoff quantification for isotropic-elastic full-waveform inversion with various model parameterizations: Geophysics, Accepted.

Pan, W., Innanen, K. A., Margrave, G. F., Fehler, M. C., Fang, X., and Li, J., 2016, Estimation of elastic constants for HTI media using Gauss-Newton and full-Newton multiparameter full-waveform inversion: Geophysics, **81**, R275–R291.

Plessix, R. E., 2006, A review of the adjoint-state method for computing the gradient of a functional with geophysical applications: Geophysical Journal International, **167**, 495–503.

Pratt, R. G., Shin, C., and Hicks, G. J., 1998, Gauss-Newton and full Newton methods in frequency-space seismic waveform inversion: Geophysical Journal International, **133**, 341–362.

Quan, Y., and Harris, J. M., 1997, Seismic attenuation tomography using the frequency shift method: Geophysics, **62**, 895–905.

Robertsson, J. O. A., Blanch, J. O., and Symes, W. W., 1994, Viscoelastic finite-difference modeling: Geophysics, **59**, 1444–1456.

Routh, P., Neelamani, R., Lu, R., Lazaratos, S., Braaksma, H., Hughes, S., Saltzer, R., Stewart, J., Naidu, K., Averill, H., Gottumukkula, V., Homonko, P., Reilly, J., and Leslie, D., 2017, Impact of high-resolution FWI in the Western Black Sea: Revealing overburden and reservoir complexity: The Leading Edge, **36**, 60–66.

Shen, Y., Biondi, B., and Clapp, R., 2018a, *Q*-model building using one-way wave-equation migration *Q* analysis - Part 1: Theory and synthetic test: Geophysics, **83**, S93–S109.

Shen, Y., Biondi, B., and Clapp, R., 2018b, *Q*-model building using one-way wave-equation migration *Q* analysis - Part 2: 3D field-data test: Geophysics, **83**, S111–S126.

Tape, C., Niu, Q., Maggi, A., and Tromp, J., 2009, Adjoint tomography of the southern caliornia crust: Science, **325**, 988–992.

Tarantola, A., 1984, Inversion of seismic reflection data in the acoustic approximation: Geophysics, **49**, 1259–1266.

Tonn, R., 1991, The determination of seismic quality factor q from vsp data: A comparison of different computational methods: Geophysical Prospecting, **39**, 1–27.

Trinh, P., Brossier, R., Métivier, L., Tavard, L., and Virieux, J., 2018, Efficient time-domain 3d elastic and visco-elastic fwi using a spectral-element method on flexible cartesian-based mesh: Geophysics.

Tromp, J., Tape, C., and Liu, Q., 2005, Seismic tomography, adjoint methods, time reversal, and banana-doughnut kernels: Geophysical Journal International, **160**, 195–216.

Virieux, A., and Operto, S., 2009, An overview of full-waveform inversion in exploration geophysics: Geophysics, **74**, WCC1–WCC26.

Warner, M., Ratclie, A., Nangoo, T., Morgan, J., Umpleby, A., Shah, N., Vinje, V., Stekl, I., Guasch, L., Win, C., Conroy, G., and Bertrand, A., 2013, Anisotropic 3D full-waveform inversion: Geophysics, **78**, R59–R80.

Yang, D., Malcolm, A., Fehler, M., and Huang, L., 2014, Time-lapse walkaway vertical seismic profile monitoring for CO_2 injection at the SACROC enhanced oil recovery filed: A case study: Geophysics, **79**, B51–B61.

Yang, P., Brossier, R., Métivier, L., Virieux, J., and Zhou, W., 2018, A Time-Domain Preconditioned Truncated Newton Approach to Visco-acoustic Multiparameter Full Waveform Inversion: SIAM Journal on Scientific Computing, **40**, B1101–B1130.

Yao, G., Silva, N. V., Warner, M., and Kalinicheva, T., 2018, Separation of migration and tomography modes of fullâĂŘwaveform inversion in the plane wave domain: Journal of Geophysical Research: Solid Earth, **123**, 1486–1501.

Yuan, Y., and Simons, F. J., 2014, Multiscale adjoint waveform-difference tomography using wavelets: Geophysics, **79**, WA79–WA95.

Zhu, H., Bozdağ, E., Duffy, T. S., and Tromp, J., 2013, Seismic attenuation beneath Europe and the North Atlantic: Implications for water in the mantle: Earth and Planetary Science Letters, **381**, 1–11.

Zhu, H., and Tromp, J., 2013, Mapping tectonic deformation in the crust and upper mantle beneath Europe and the North Atlantic Ocean: Science, **341**, 871–875.

Zhu, T., 2014, Seismic modeling, inversion and imaging in attenuating media: Ph.D. thesis, Stanford University.

Zhu, T., and Harris, J. M., 2015, Improved seismi image by *Q*-compensated reverse time migration:Application to crosswell field data, west texas: Geophysics, **80**, B61–B67.

Zhu, T., Harris, J. M., and Biondi, B., 2014, *Q*-compensated reverse-time migration: Geophysics, **79**, R471–R484.

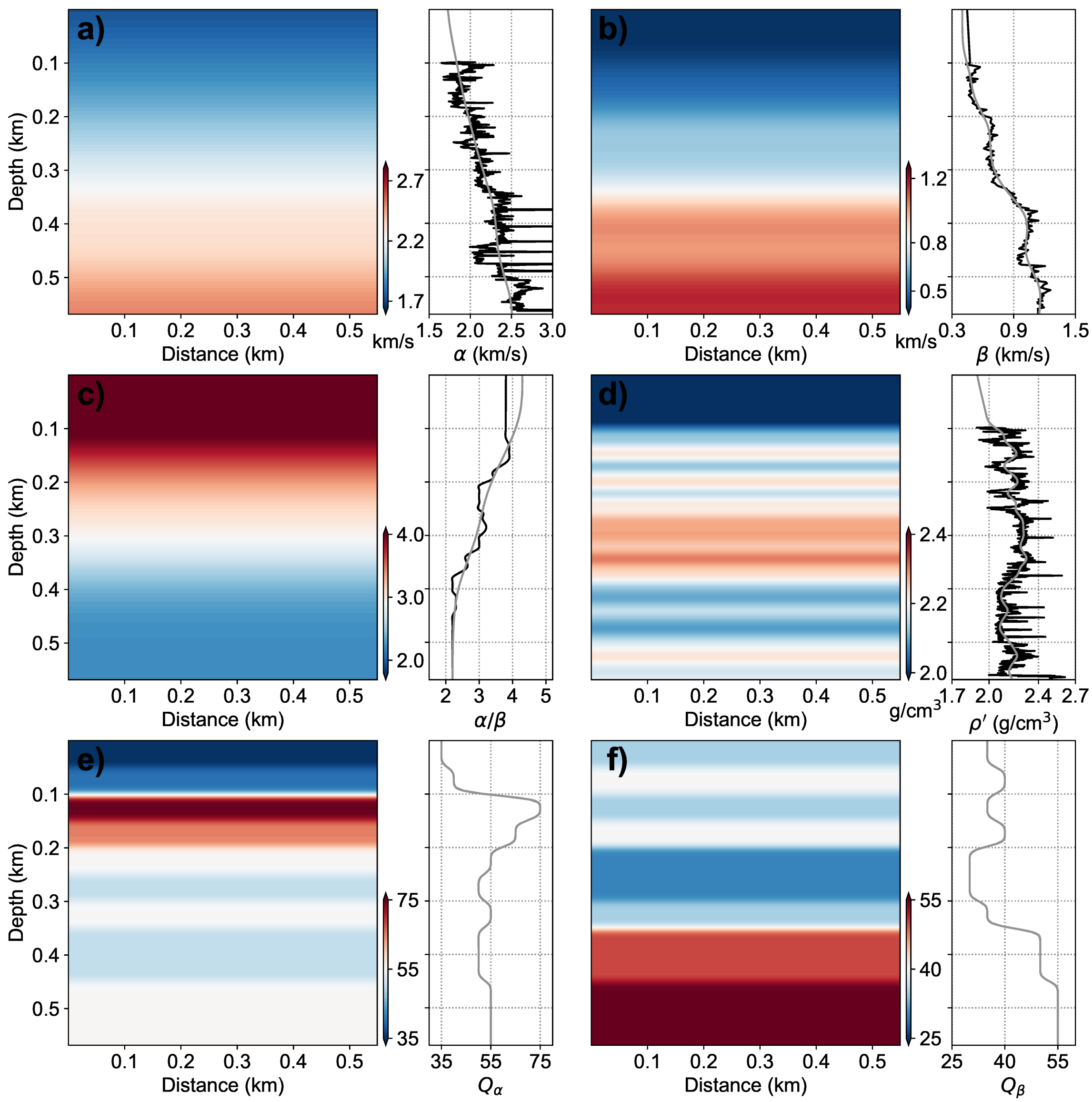

FIG. 10. (a-d) are the initial α, β, α/β ratio and ρ' models; (e-f) are the initial Q_α and Q_β models. At each sub-panel, the black and gray lines indicate the well-log data and initial models, respectively.

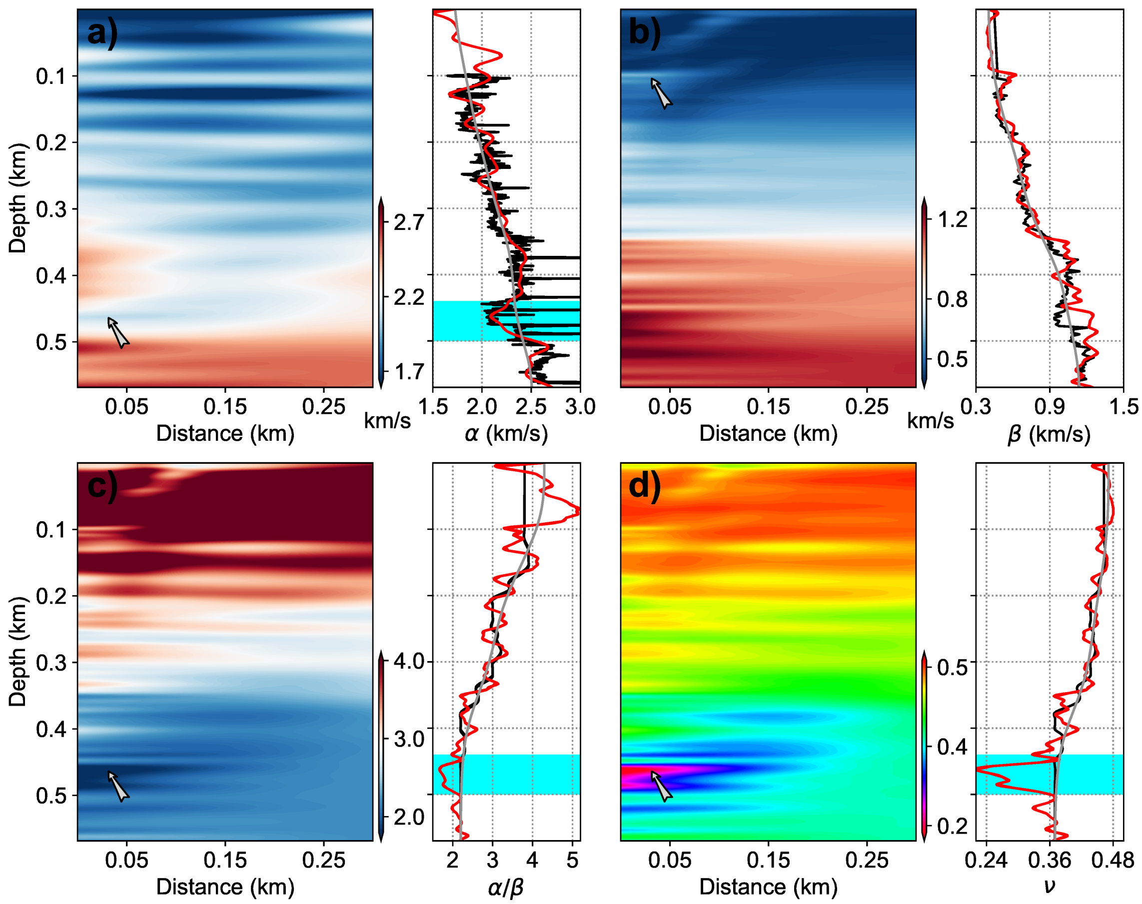

FIG. 11. (a-d) are the inverted α, β, derived α/β ratio and Poisson's ratio ν models in the stage-I inversion experiment. At each sub-panel, the black, gray and red lines indicate the well-log data, initial models and inverted models.

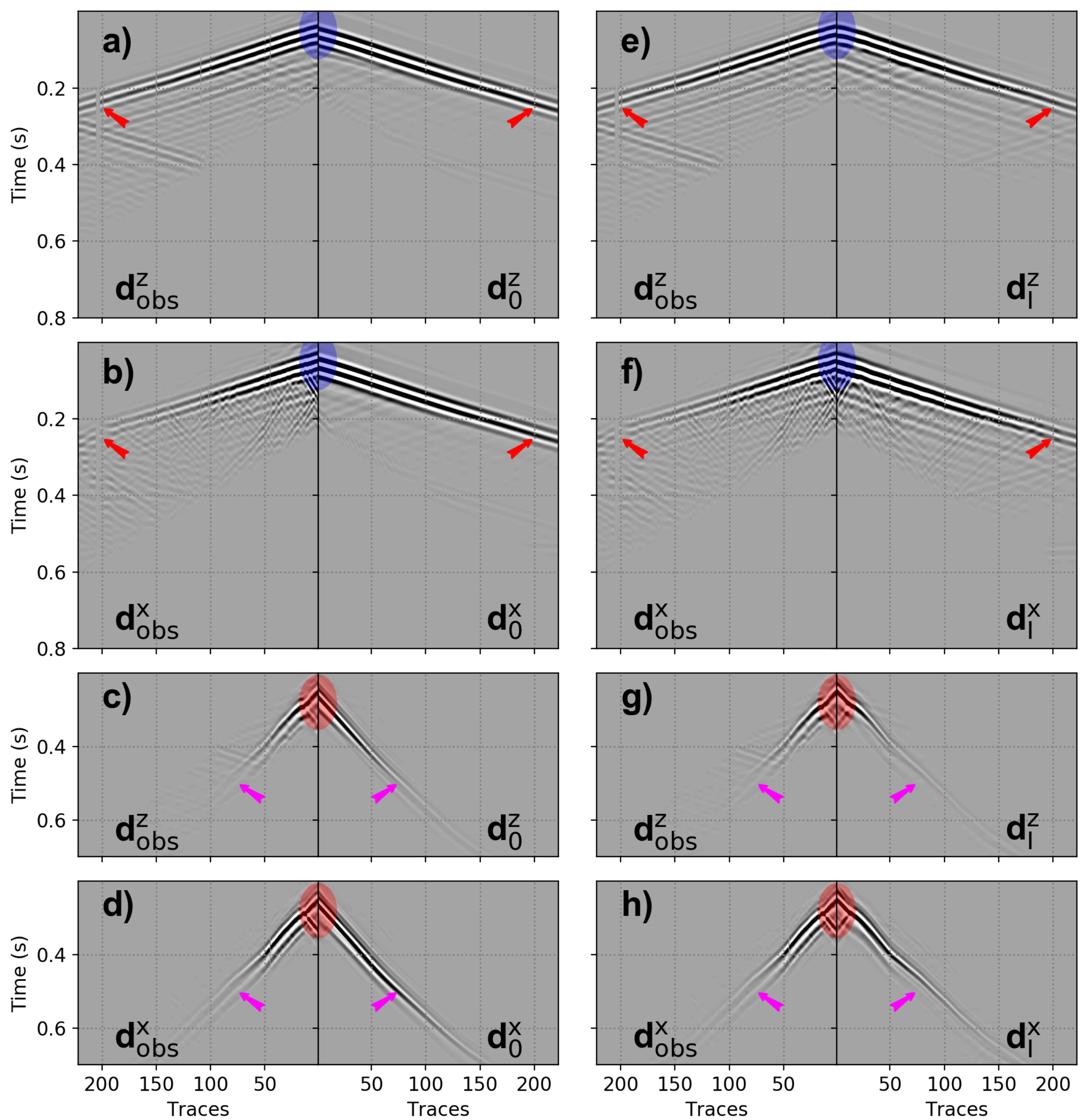

FIG. 12. (a-b) show the comparison of the z and x component observed data ($\mathbf{d}^z_{\text{obs}}$ and $\mathbf{d}^x_{\text{obs}}$) with synthetic data ($\mathbf{d}^z_0$ and $\mathbf{d}^x_0$) calculated from the initial models in time window Tb; (c-d) show the comparison of the z and x component observed data with synthetic data calculated from the initial models in time window Ta; (e-h) show the comparison of the observed data with the synthetic data ($\mathbf{d}^z_{\text{I}}$ and $\mathbf{d}^x_{\text{I}}$) calculated from the stage-I inverted models in time windows Tb and Ta.

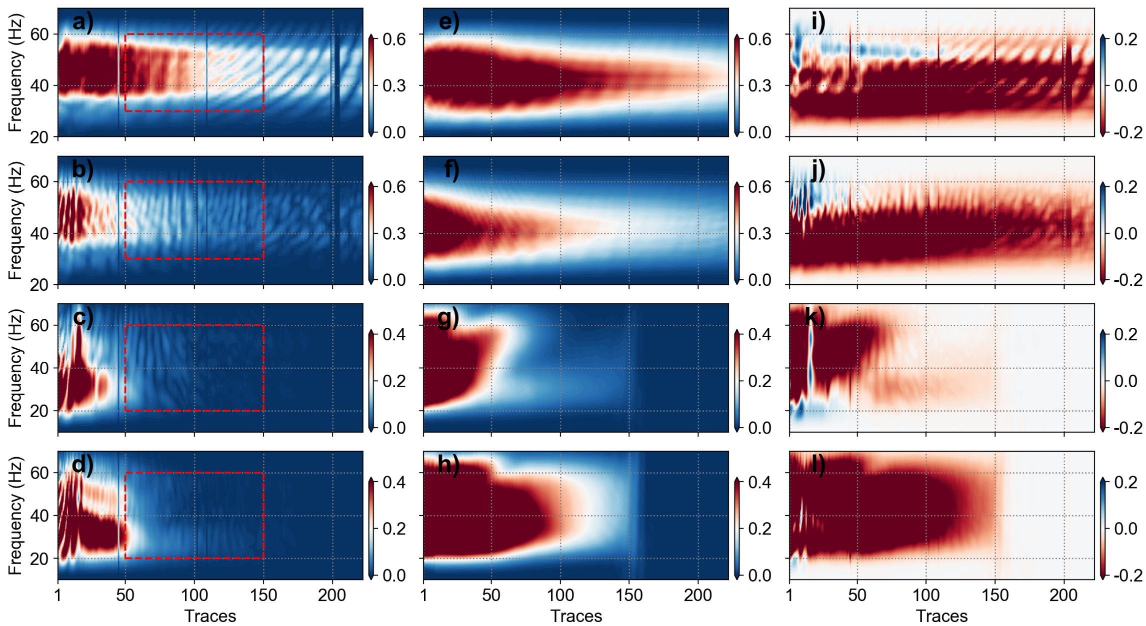

FIG. 13. (a-b) are the amplitude spectrum of down-going P-waves of z and x component observed data in time window Tb (plotting frequency range 20-70 Hz); (c-d) are the amplitude spectrum of down-going S-waves of z and x component observed data in time window Ta (plotting frequency range 10-70 Hz); (e-h) are the amplitude spectrum of z and x component synthetic data calculated from the initial models; (i-l) are the corresponding amplitude spectrum differences.

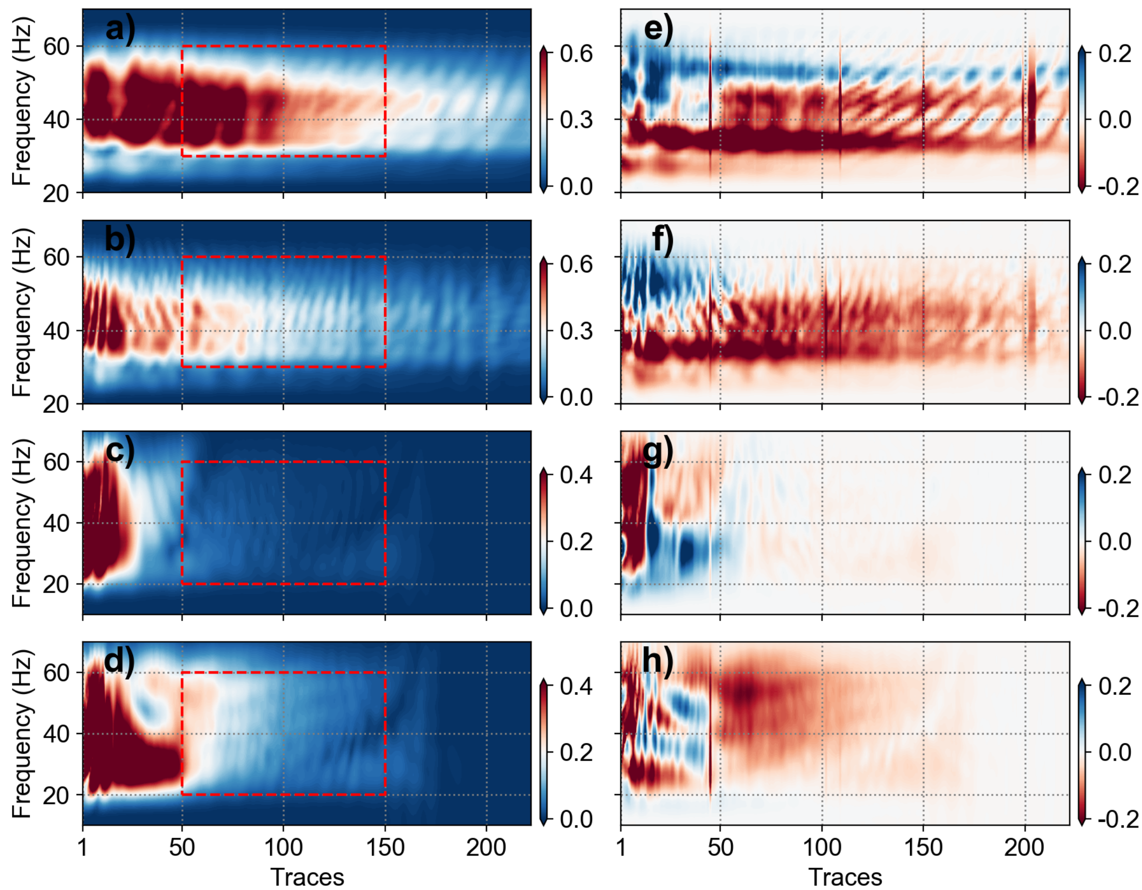

FIG. 14. (a-d) are the amplitude spectrum of down-going P- and S-waves of z and x component synthetic data calculated from the stage-I inverted models in time windows Tb and Ta; (e-h) are the amplitude spectrum differences between the stage-I synthetic data and observed data.

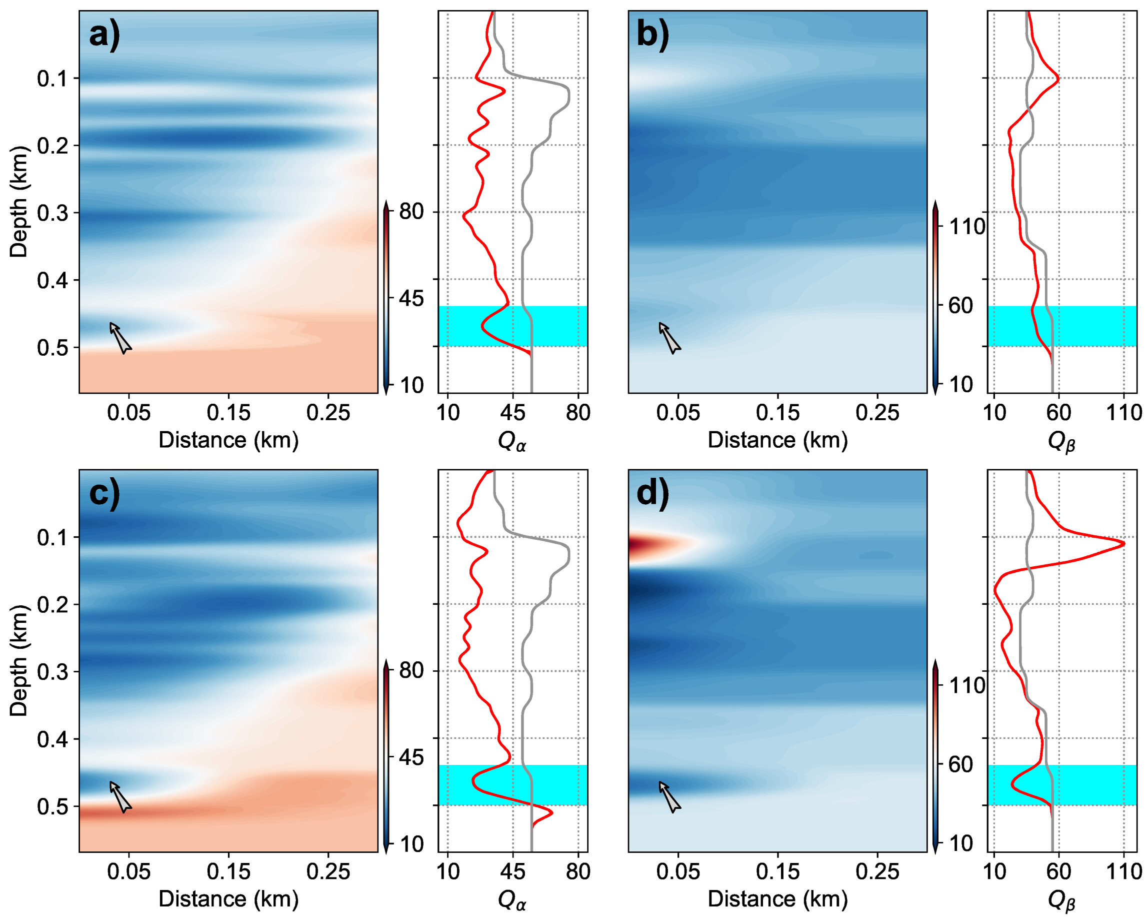

FIG. 15. (a-b) are the inverted Q_α and Q_β models using the traditional WD misfit function; (c-d) are the inverted Q_α and Q_β models using the I-AR misfit function.

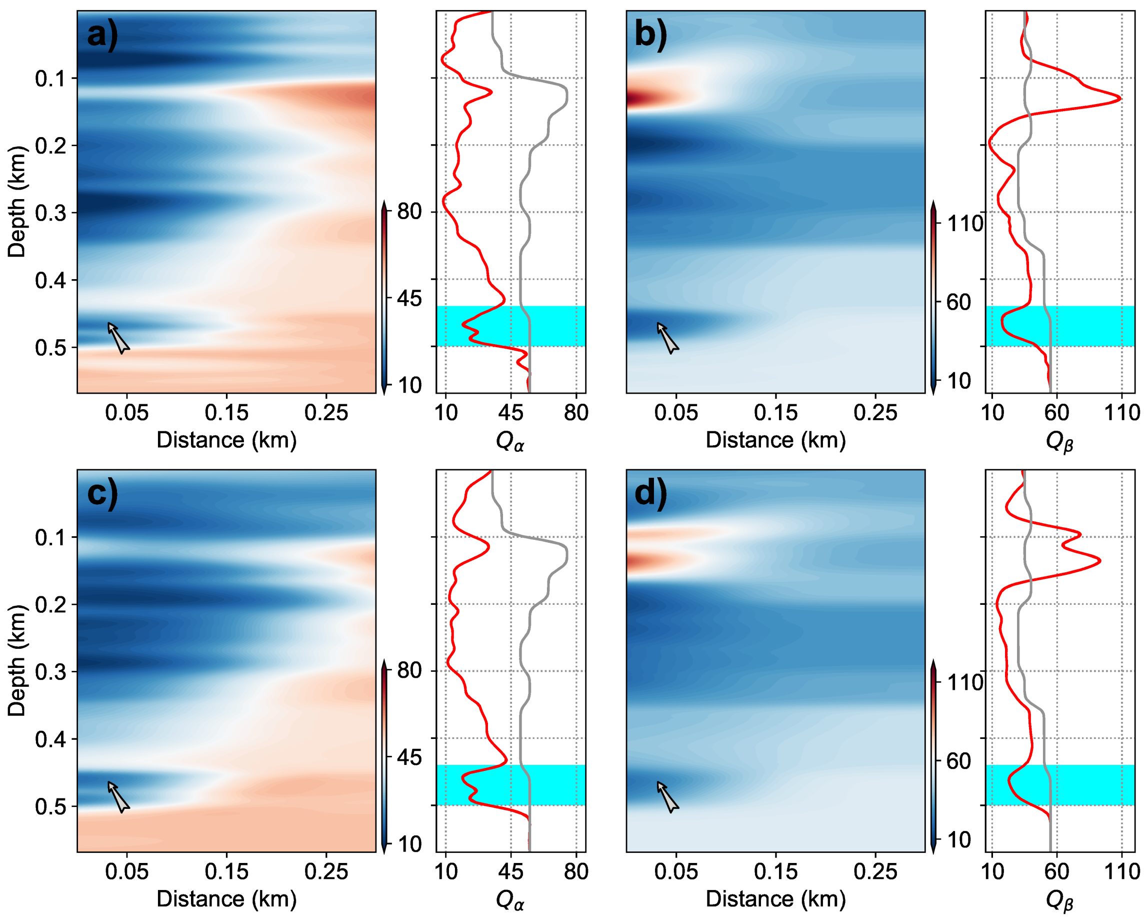

FIG. 16. (a-b) are the inverted Q_α and Q_β models using the RMS-AR misfit function; (c-d) are the inverted Q_α and Q_β models using the S-AR misfit function.

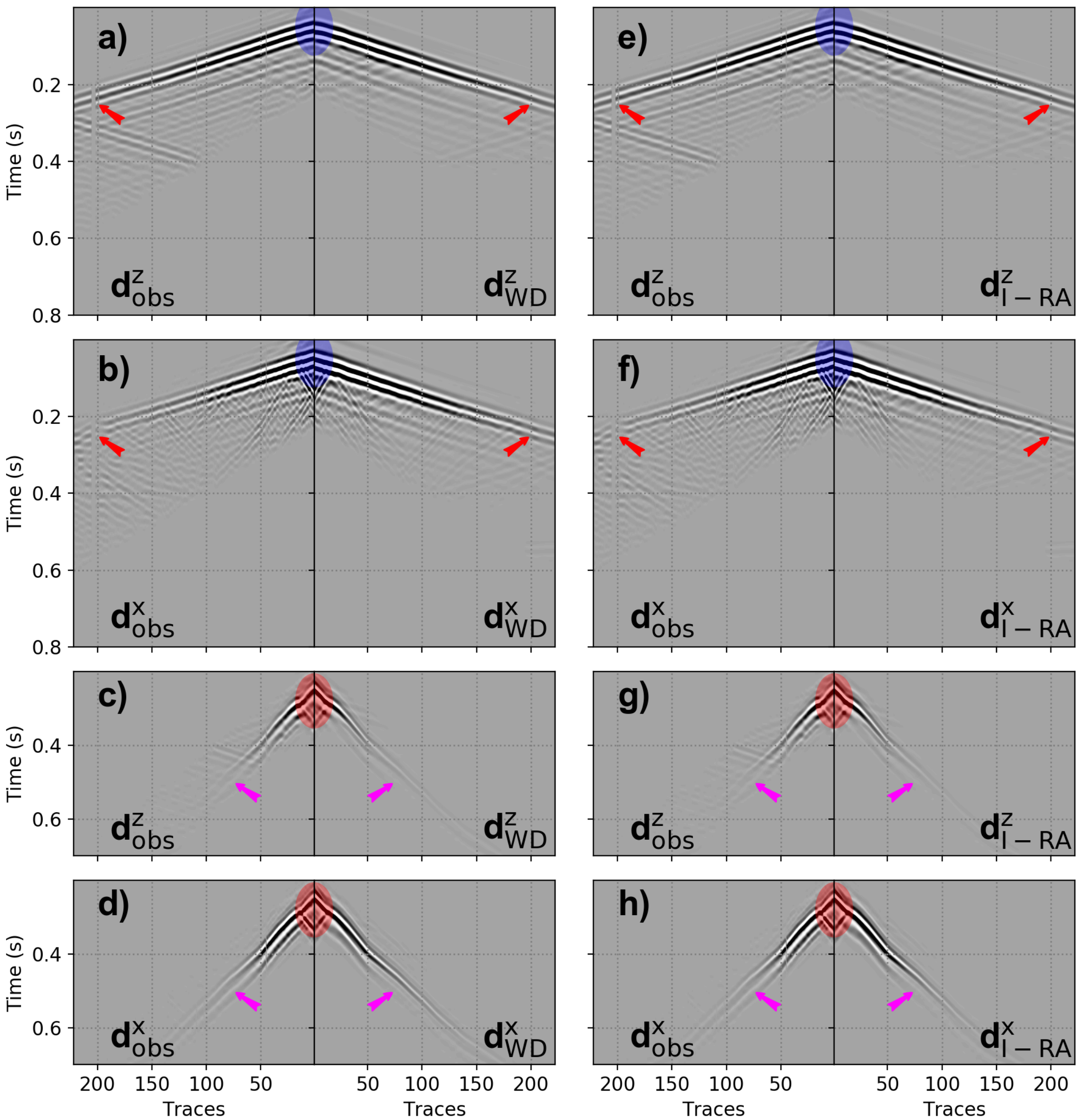

FIG. 17. (a-d) show the comparison of the observed data with the synthetic data calculated from the inverted attenuation models by the WD misfit function; (f-h) show the comparison of the observed data with the synthetic data calculated from the I-AR misfit function inverted attenuation models

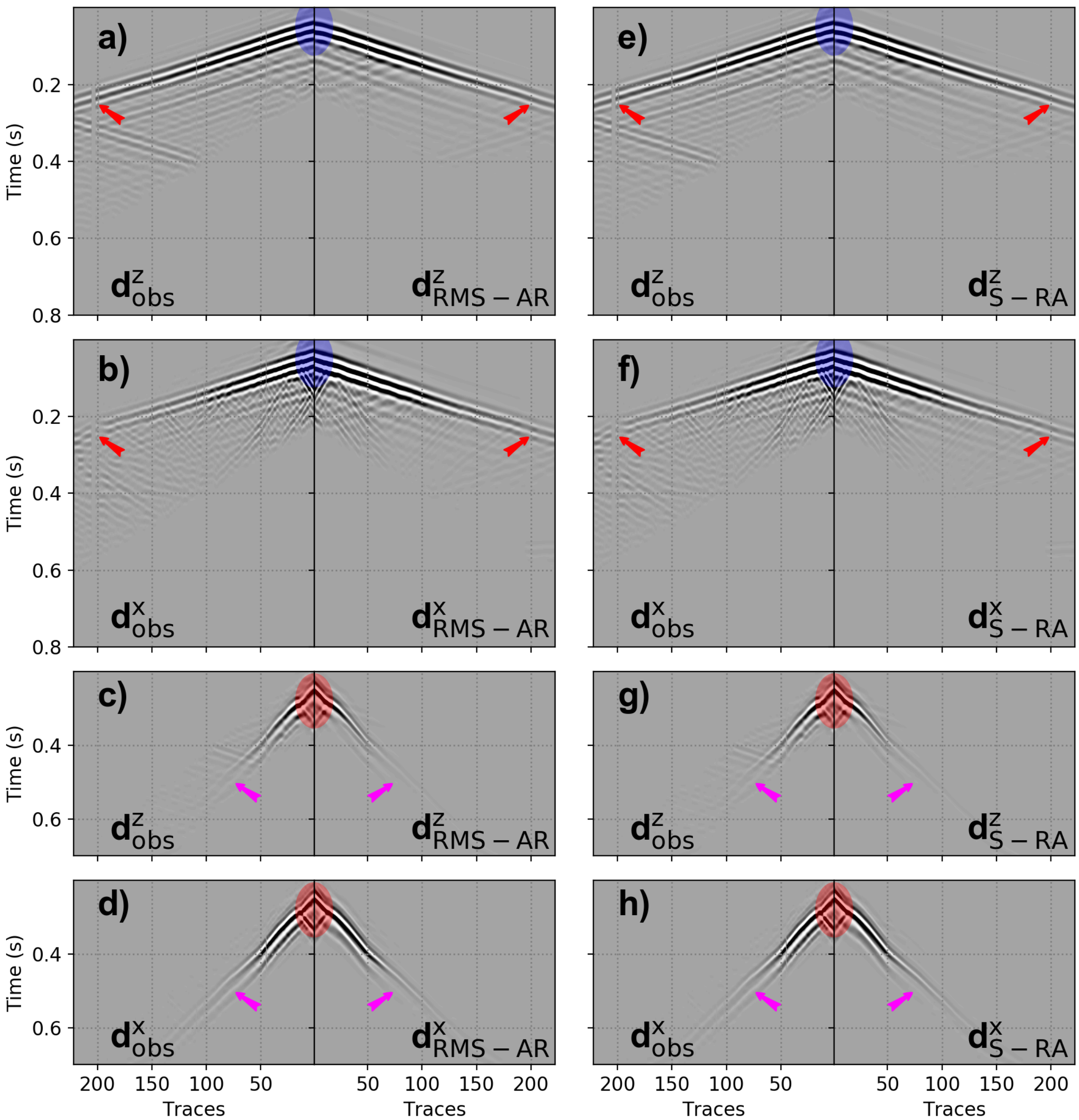

FIG. 18. (a-d) show the comparison of the observed data with the synthetic data calculated from the RMS-AR misfit function inverted attenuation models; (f-h) show the comparison of the observed data with the synthetic data calculated from the S-AR misfit function inverted attenuation models.

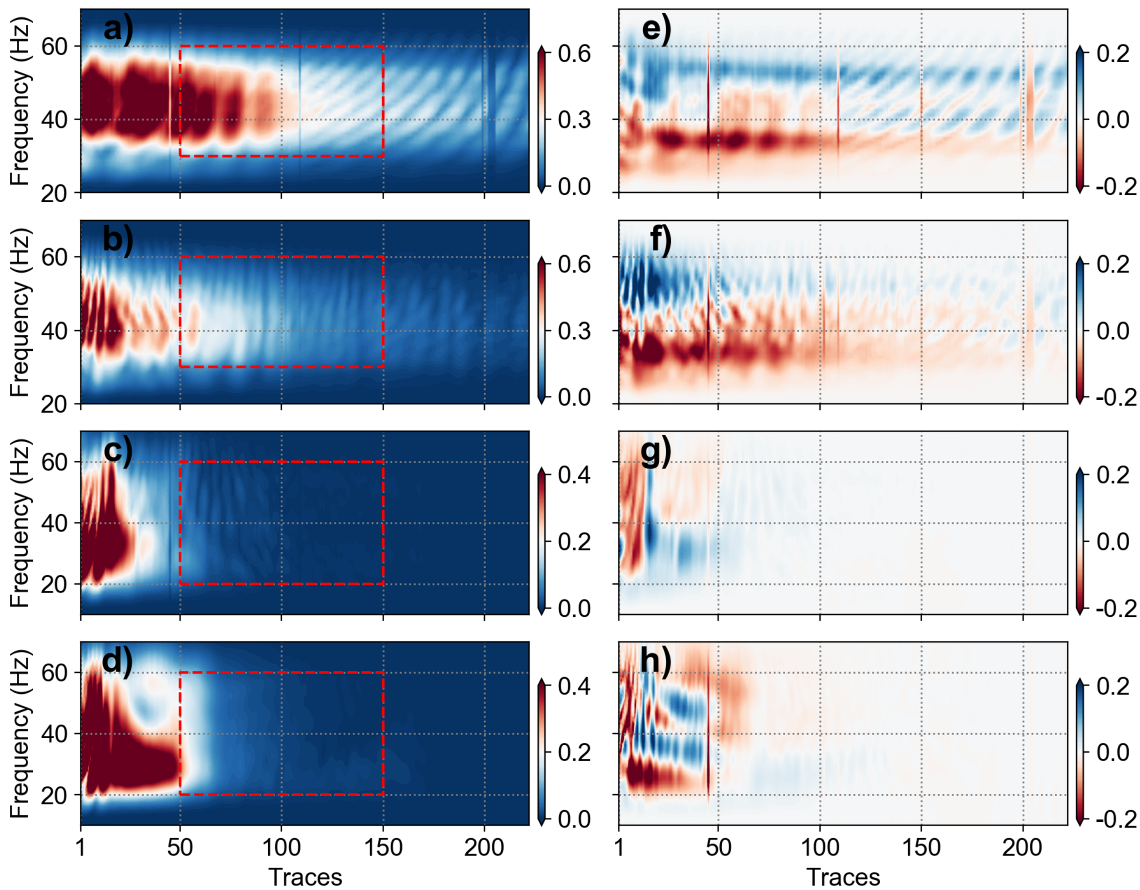

FIG. 19. (a-d) are the amplitude spectrum of down-going P- and S-waves of z and x component synthetic data calculated from the stage-II inverted attenuation models in time windows Tb and Ta; (e-h) are the amplitude spectrum differences between the stage-II synthetic data and observed data.

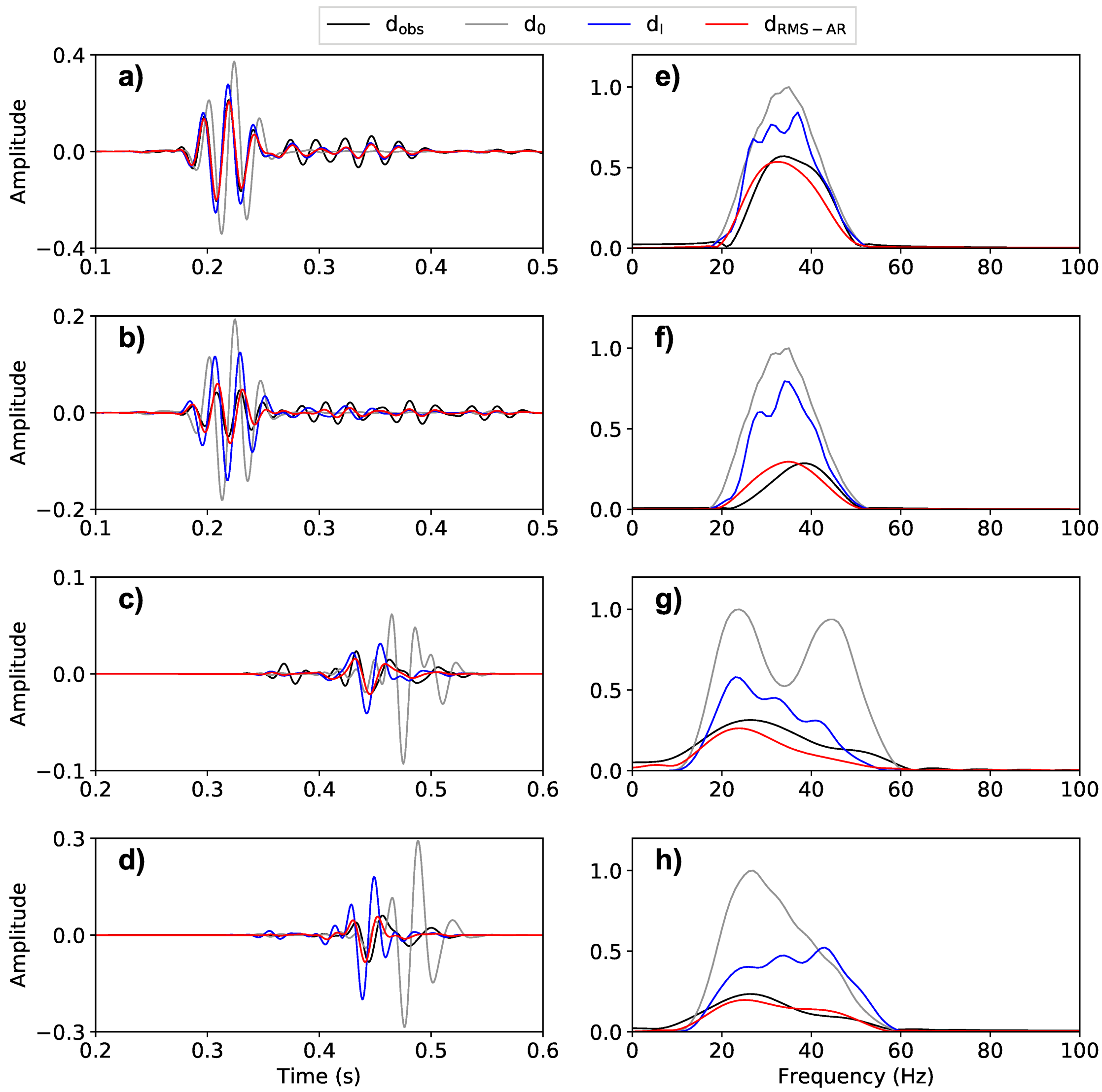

FIG. 20. (a-b) are the comparison of the trace 180 of down-going P-wave in z and x component observed data and synthetic data (time window Tb); (c-d) are the comparison of the trace 70 of down-going S-wave in z and x component observed data and synthetic data (time window Ta). (e-h) are the corresponding amplitude spectrum with Gaussian smoothing. The black and gray lines indicate the observed data ($\mathbf{d}_{\mathrm{obs}}$) and initial synthetic data ($\mathbf{d}_0$). The blue and red lines indicate the stage-I synthetic data ($\mathbf{d}_{\mathrm{I}}$) and the stage-II synthetic data ($\mathbf{d}_{\mathrm{RMS-AR}}$).

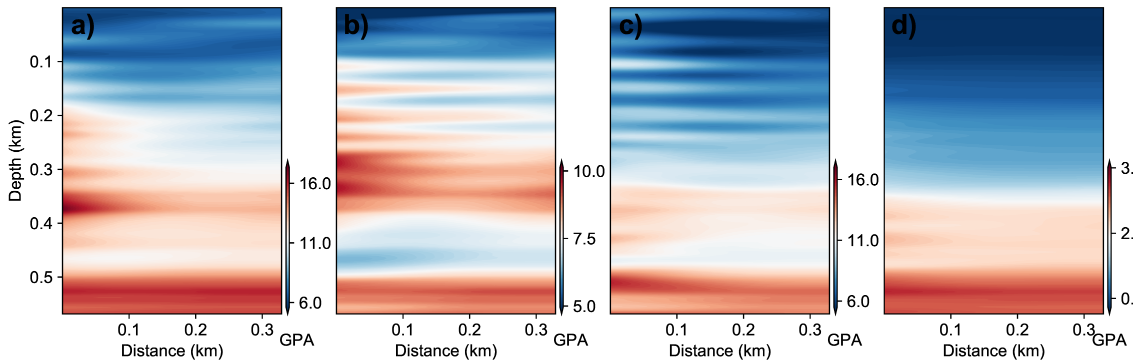

FIG. 21. The inverted models of c_{11} (a), c_{13} (b), c_{33} (c) and c_{55} (d) using the elastic-constant model parameterization.

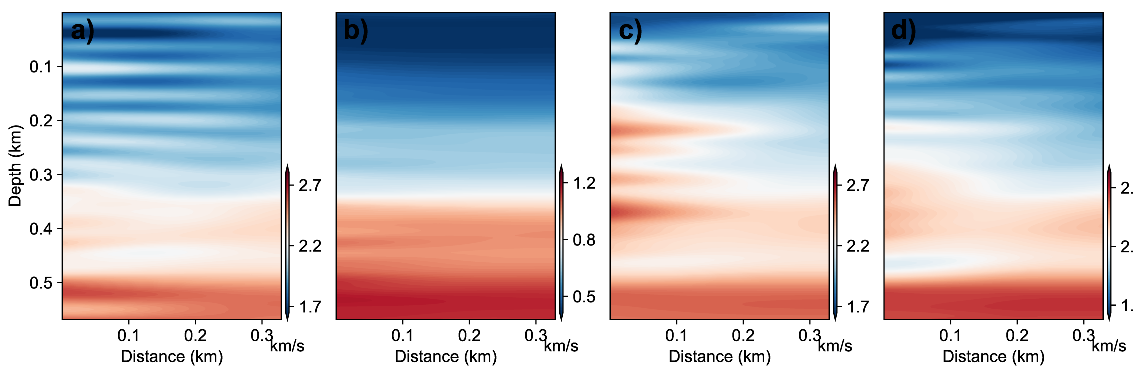

FIG. 22. The inverted models of α (a), β (b), α_h (c) and α_{nmo} (d) using the VTI-velocity model parameterization.

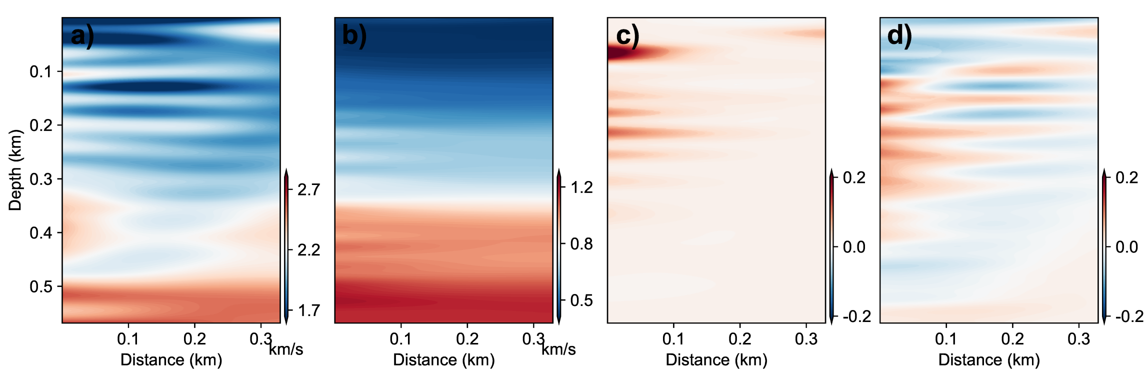

FIG. 23. The inverted models of α (a), β (b), ε (c) and δ (d) using the velocity-Thmosen-I model parameterization.

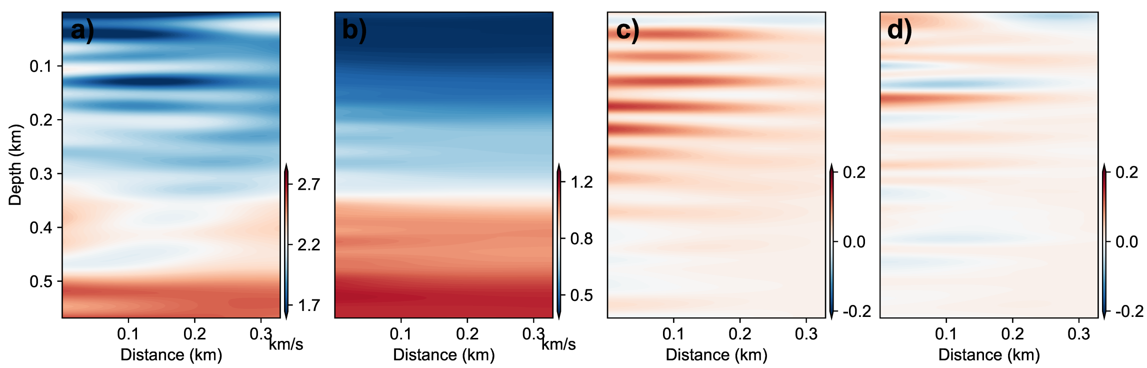

FIG. 24. The inverted models of α_h (a), β (b), ε (c) and η (d) using the velocity-Thmosen-II model parameterization.